

Theoretical Design of Surface Plasmon Resonance based Microwave Sensor using Optical Fiber

by

Imran Khan

A thesis submitted in partial fulfillment of the requirements for the degree of
Master of Science in Electronics and Communication Engineering



Khulna University of Engineering & Technology
Khulna 9203, Bangladesh

September 2014

Declaration

This is to certify that the thesis work entitled "*Theoretical Design of Surface Plasmon Resonance based Microwave Sensor using Optical Fiber*" has been carried out by *Imran Khan* in the Department of Electronics and Communication Engineering, Khulna University of Engineering & Technology, Khulna, Bangladesh. The above thesis work or any part of this work has not been submitted anywhere for the award of any degree or diploma.



Signature of Supervisor

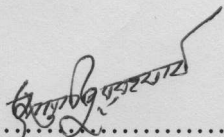
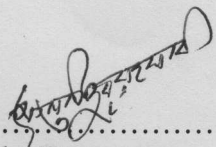
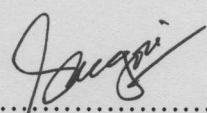
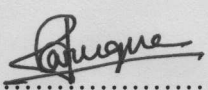
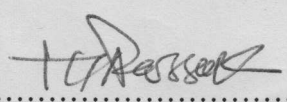


Signature of Candidate

Approval

This is to certify that the thesis work submitted by *Imran Khan* entitled "*Theoretical Design of Surface Plasmon Resonance based Microwave Sensor using Optical Fiber*" has been approved by the board of examiners for the partial fulfillment of the requirements for the degree of *Master of Science in Electronics and Communication Engineering* at *Khulna University of Engineering & Technology, Khulna, Bangladesh* in *September 2014*.

BOARD OF EXAMINERS

1. 
.....
Name: Dr. Md. Mostafizur Rahman
Designation: Professor
University: Khulna University of Engineering & Technology
Chairman
(Supervisor)
2. 
.....
Head of the Department
Department of Electronics & Communication Engineering
Khulna University of Engineering & Technology
Member
3. 
.....
Name: Dr. Md. Osman Goni
Designation: Professor
University: Khulna University of Engineering & Technology
Member
4. 
.....
Name: Dr. Md. Faruque Hossain
Designation: Associate Professor
University: Khulna University of Engineering & Technology
Member
5. 
.....
Name: Dr. S. M. Abdur Razzak
Designation: Professor
University: Rajshahi University of Engineering & Technology
Member
(External)

Acknowledgement

The author acknowledges the support by the Electronics and Communication Engineering Department, Khulna University of Engineering & Technology (KUET), Bangladesh; Photonics Department, Vrije Universiteit Brussel (VUB) & Ghent University, Belgium and Microwave Photonics Laboratory, University of Ottawa, Canada. He also likes to thank Prof. F. Berghmans, Prof. J. Yao, S. Lambert, C.W.Oh, J. B. Martinez, T. Baghdasaryan and Y. Chowdhury for their support.

Abstract

Microwaves (MW) sensing is done through a complex and large size sensor which comprises a lot of electronic components. In this research, microwave (MW) sensing, based on surface plasmon resonance using optical fiber is analyzed and a new scheme to sense MW is proposed. The motivation is to introduce a new scheme to sense MW, minimize the conventional MW detector size and reduce the number of electronic components in the sensor by using a new scheme. Here MW is detected by measuring the surface plasmon wavelength shift which is the result of the related Bragg wavelength shift ($0.009 \text{ nm}/^{\circ}\text{C}$) in the optical fiber due to temperature change. The results are compared with existing research findings to establish the sensing principle of MW based on surface plasmon resonance, generated in optical fiber's metal-dielectric interface. This proposed sensor can be integrated with other micro-electronic devices very easily.

Contents

	PAGE
Title Page	i
Declaration	ii
Approval	iii
Acknowledgement	iv
Abstract	v
Contents	vi
List of Tables	viii
List of Figures	ix
List of Illustrations	xi
CHAPTER I	
Introduction	1
1.1 Surface Plasmons	1
1.2 Surface Plasmon Resonance	2
CHAPTER II	
Literature Review	4
CHAPTER III	
Idea & Methodology	7
3.1 SPR based Tilted Fiber Bragg Grating Sensor	7
3.2 Microwave Interaction with Metals	8
3.3 Microwave Detection Possibility	10
CHAPTER IV	
Experiment & Results	13
4.1 Experiment for Uniform FBG	13

	4.2 Experimental Data for Uniform FBG	14
	4.3 Calculation of Error for Uniform FBG	16
	4.4 Experiment for Chirped Fiber Bragg Grating	17
	4.5 Experimental Data for Chirped FBG	18
	4.6 Calculation of Error for Chirped FBG	19
CHAPTER V	Discussion	21
CHAPTER VI	Analysis	24
	6.1 Waveguide with SOI Material System	28
	6.2 Waveguide with SOS Material System	32
CHAPTER VII	Efficient Design Considerations	36
	7.1 Effect of ARC for SOI Material System	39
	7.2 Effect of ARC for SOS Material System	47
CHAPTER VIII	Conclusion & Future Works	55
	References	56

LIST OF TABLES

Table No.	Description	Page
4.1	Experimental Data for uniform FBG	14
4.2	Data for Error Calculation of FBG	16
4.3	Experimental Data for CFBG	18
4.4	Data for Error Calculation of CFBG	20
6.1	Microwave frequency and Depth of penetration	24
6.2	Effective index of the fundamental and first order mode as a function of WG width for SOI	29
6.3	Effective index and loss as a function of the radius of the bend for SOI	31
6.4	Effective index of the fundamental and first order mode as a function of WG width for SOS	32
6.5	Effective index and loss as a function of the radius of the band for SOS	33
7.1	Dimensions of the Gaussian field profile for SOI	41
7.2	Dimensions of the Gaussian field profile for SOS	48
7.3	Multilayer coating design for SOS	53

LIST OF FIGURES

Figure No.	Description	Page
1.1	Plasma oscillation in the conductor	2
1.2	Localized SPR when field (light) interacts with the plasmons	3
2.1	Fiber Bragg Grating, refractive index modulation and spectral response	5
3.1	SPR based TFBG sensor principle	7
3.2	Microwave-Metal interaction	8
3.3	Change in temperature of thin Au film with a thickness of 34.6 nm (left figure) and 29.5 nm (right figure) during microwave irradiation	9
3.4	Microwave effect on Au film with different thicknesses T1=45 nm, T2=133 nm & T3=407 nm (a) for H-field (b) for E-field	9
4.3	Bragg wavelength dependence on temperature	15
4.4	Experimental results of the Bragg wavelength dependence on temperature and linear fitting	15
4.5	Observed Bragg wavelength in Optical Spectrum Analyzer	16
4.6	Bragg wavelength dependence on temperature and linear fitting for CFBG.	19
5.1	SPR and Bragg wavelength shift due to temperature change	21
5.2	Proposed MW sensor using TFBG	22
5.3	SPR wavelength shift corresponding to the refractive index change	23
6.1	Microwave frequency vs penetration depth for Au metal film	25
6.2	SNR vs. Ag-Au alloy film thickness	26
6.3	Sensitivity vs. Ag-Au alloy film thickness	26
6.4	SPR based Hetero-core structured optical fiber sensor	27
6.5	Bended waveguide with fixed radius and thin gold layer	28
6.6	n_{eff} of different modes as a function of the WG width for SOI	29

6.7	Losses as a function of the radius for the WG bend in case of SOI	31
6.8	n_{eff} as a function of the radius of the WG bend in case of SOI	31
6.9	n_{eff} of the different modes as a function of the width for SOS	32
6.10	Losses as a function of the radius for the WG bend in case of SOS	33
6.11	n_{eff} as a function of the radius of the WG bend in case of SOS	34
6.12	Polarization independence characteristics of the symmetrical DLUWT	35
7.1	Chirped grating	36
7.2	Proposed MW sensor using Tilted Chirped FBG concept	38
7.3	Waveguide facets for SOI material system	40
7.4	Transmission for all polarizations when there is no coating: magnitude (solid lines) and phase (dashed lines). TM: red, TE: blue, Mean: green	42
7.5	Input field amplitude	43
7.6	Output field amplitude (mean)	43
7.7	Output field amplitude (Mean)	45
7.8	Transmission for all polarisations for a single layer coating: magnitude (solid lines) and phase (dashed lines). TM: red, TE: blue, Mean: green	45
7.9	Cross-section of a waveguide fabricated in silica on silicon	48
7.10	Transmission for all polarisations when there is no coating: magnitude (solid lines) and phase (dashed lines). TM: Red, TE: Blue, Mean: Green.	49
7.11	Input field amplitude	50
7.12	Output field amplitude (mean)	52
7.13	Transmission for all polarisations for a 1 layer coating: magnitude (solid lines) and phase (dashed lines). TM: Red, TE: Blue, Mean: Green.	52
7.14	Output field amplitude (mean).	53
7.15	Proposed MW sensor using TCFBG concept and ARC materials as cladding.	54

LIST OF ILLUSTRATION

Illustration No.	Description	Page
3.5	Flowchart for the proposed MW detection scheme using Tilted FBG	11
3.6	Flowchart for the proposed MW detection scheme using Tilted Chirped FBG concept	12
4.1	Experimental setup	13
4.2	Practical work bench	14

CHAPTER I

Introduction

When guided light inside a fiber is modified by external physical, mechanical, chemical or biological influences of the surrounding environment, the change can be detected by measuring the characteristics of the output light. The optical fiber (OF) for sensor application is designed in such a way so that there is a short portion in the fiber where the core refractive index is different from the usual fiber core and cladding refractive index [1]. This is the basic construction of fiber optic sensors. One of the recent schemes for sensing using fiber optics is the surface plasmon resonance (SPR). This type of sensor is now widely used in case of bio-sensing [2], [3] and in many other sensing applications [4]-[6]. For the generation of SPR in the fiber optics it is necessary to use the metallic layer on the fiber. Microwaves (MW) can penetrate metal in the order of nanometer range and can increase the heat inside the metal. Thus it is possible to sense the surface plasmon wavelength shift due to the heat caused by MW penetration. Therefore, there is the possibility to detect MW frequencies using SPR based sensors by observing the related SPR wavelength shift with respect to the reference SPR wavelength.

1.1 Surface Plasmons

Inside a conductor such as metals, a lot of free electrons are available and these electrons can be considered as plasma particles. At the same time there are equal numbers of positive charged ions from lattice so the total charge density in the conductor is zero.

Now if an external field is applied then the electrons will start to move. The electrons will move towards the positive region and at the same time the positive ions will be moving as opposite to the electrons. Due to this moving mechanism a longitudinal oscillation will be introduced in the conductor and this phenomenon is known as the plasma oscillation [7] as shown in Fig. 1.1 [9].

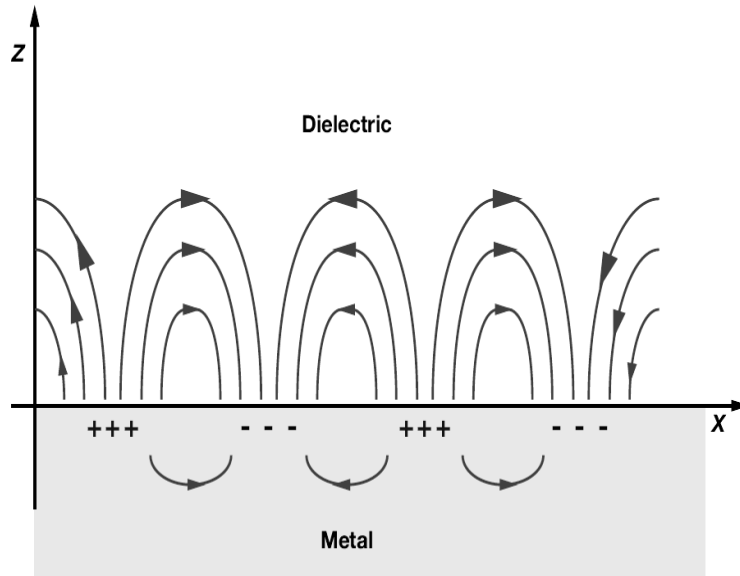


Figure 1.1: Plasma oscillation in the conductor [9].

1.2 Surface Plasmon Resonance

To support the surface plasma to oscillate, an interface of a conductor and a dielectric is required. In general a metal and dielectric interface is used to support the surface plasmon oscillation. Due to this oscillation a surface plasmon wave is generated as shown in Fig. 1.2 [9]. This surface plasmon is only TM polarized electromagnetic field because for TE polarized case there is no solution of the Maxwell's equation. So for surface plasmon wave only TM polarized electric field exists. This wave is decayed exponentially in the metal. This Surface Plasmon Wave (SPW) is characterized by the propagation constant as mentioned below [7], [8]-

$$\beta = \frac{\omega}{c} \sqrt{\frac{\epsilon_M \epsilon_D}{\epsilon_M + \epsilon_D}} \quad (1.1)$$

where ω is the angular frequency, c is the speed of light in vacuum, ϵ_M and ϵ_D are dielectric permittivities for metal and dielectric respectively. So from (1.1) we can say that the property of the SPW is dependent on the property of the two materials i.e. the metal and dielectric media.

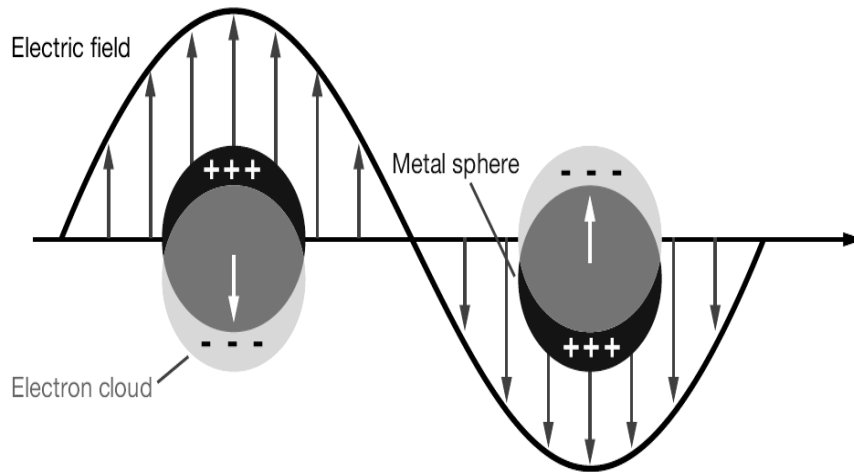


Figure 1.2: Localized SPR when field (light) interacts with the plasmons [9].

Now to create the surface plasmon oscillation we have to excite the electrons in the conductor. So we need to impinge EM field (light) on the surface. We know that the electrical permittivity for the conductor (metal) is negative and the electrical permittivity for the dielectric is positive. In the dielectric medium the propagation constant (maximum) can be written as [7]-

$$\beta = \frac{\omega}{c} \sqrt{\epsilon_s} \tag{1.2}$$

We can say that the propagation constant for surface plasmon wave is higher than the propagation constant of light in the dielectric medium. As a result we cannot excite the surface plasmon with normal light; we need to use the light with extra momentum or energy with the same polarization state as the surface plasmon wave. Moreover the propagation constant should be matched with the surface plasmon wave.

CHAPTER II

Literature Review

Specially designed Optical Fiber (OF) can be worked as a sensor. The OF for sensor application is designed in such a way so that there is a short portion in the fiber where the core refractive index is different from the usual fiber core and cladding refractive index [1]. Normally, a periodic structure is introduced in that short portion of the OF core. This portion of the fiber core reflects the light of a specific wavelength & generally known as Fiber Bragg Gratings (FBG). A type of Distributed Bragg Reflector (DBR) constructed in a short segment of Optical Fiber that reflects the light of a particular wave length (known as Bragg wavelength) and transmit all others is known as FBG. Where DBR is a structure formed from multiple layers of alternating materials with varying refractive index, or by periodic variation of some characteristic (such as height) of a dielectric waveguide, resulting in periodic variation in the effective refractive index in the guide [10]. In other way we can say that FBG is periodic wavelength scale variation of refractive index inscribed in the segment of the fiber core. Bragg gratings reflect the light at a particular wavelength which satisfies Bragg condition. A sensor whose sensitivity is based on the Bragg wavelength shift of the Fiber Bragg Gratings is known as FBG based sensors. This reflection in a grating occurs as coupling between forward and back propagation modes at certain wavelength take place [11]. The coupling coefficient of the modes is maximum when special condition (Bragg condition) between wave vectors of light and vector number of the grating is satisfied:

$$m \cdot \lambda_B = 2 \cdot n_{eff} \cdot \Lambda \quad (2.1)$$

where λ_B is the wavelength of light called Bragg wavelength, Λ is grating period, n_{eff} is effective refractive index of the core and m is the diffraction order. The operation principle of fiber Bragg grating is illustrated in Fig. 2.1.

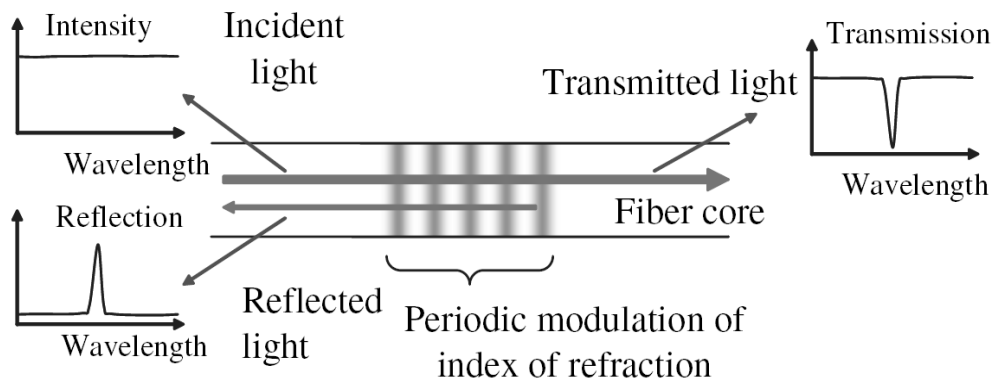


Figure 2.1: Fiber Bragg Grating, refractive index modulation and spectral response [10]

For a single FBG theoretically there exists infinite number of Bragg wavelength. It can be clearly seen from (2.1), as for different values of m , i.e. diffraction order Bragg wavelength are different. These Bragg wavelengths are separated from each other by quite large spectral range, so on practice only one (first or sometimes second) Bragg resonance wavelength is being used. For instance, when the first Bragg wavelength of the grating ($m=1$) is 1550 nm, then the second one is twice less: 750 nm. While the spectral range of sources used for fiber usually doesn't exceed 100 nm.

Additional Bragg peaks can occur if the modulation of the refractive index in FBG is not sinusoidal (which is usually the case). For instance in case of rectangular grating, the Fourier spectrum the latter has a number of modulation frequencies, which can results in several Bragg peaks. Even though most of the gratings inscribed in fiber has nearly sinusoidal index modulation.

It is also possible to change the effective index of the guided mode using the evanescent wave interaction [12]. The first demonstration of evanescent wave interaction with FBG was illustrated for a chemical transducer [13]. Further research on this type of sensor was done in [14]-[19]. Thinned FBG was introduced in [20]; a portion of the cladding layer was lifted off so that the evanescent wave can interact with the cladding mode properly.

Micro structured FBGs was introduced in [21], this structure is designed with a localized stripping of the cladding layer with radial symmetry along the grating structure.

Another type of chemical sensor was designed using palladium with FBG. The sensing principle was the swelling of the Pd-coating, resulting in a stress on the grating [22]-[25].

The Tilted FBG (TFBG) was proposed by using the idea that the transmission spectrum varies because of the cladding modes resonance sensitivity to the surroundings. The core mode couples to the cladding modes [26]-[32].

A novel idea was illustrated in 2007 by using the surface plasmon resonance with the TFBG [33]. The theory of TFBG is valid here i.e. the core mode couples to the cladding modes and resonance occurs of the surface plasmon waves.

CHAPTER III

Idea & Methodology

3.1 SPR based Tilted Fiber Bragg Grating Sensor

Recently Tilted Fiber Bragg Grating (TFBG) is used as a sensor based on the SPR principle. A small portion of the cladding of the fiber was removed and a metal film was deposited (either gold or silver) at that place so that the surface plasmon can exist at the interface of the metal dielectric (Fig. 3.1) as reported in [33]. Here the Bragg grating is tilted so that the guided mode can couple to cladding mode and as a result it can excite the surface plasmon waves. The tilting of the Fiber Bragg Grating (FBG) is done in such a way that the phase matching condition is fulfilled for the surface plasmon waves.

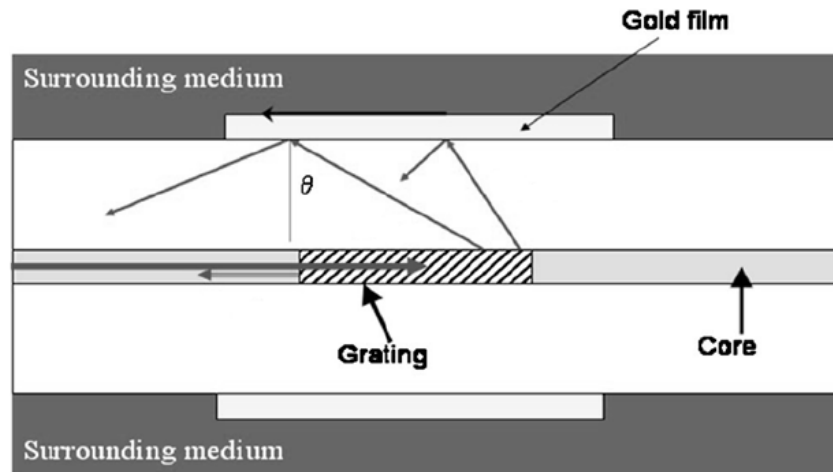


Figure 3.1: SPR based TFBG sensor principle (Reprinted with permission [33]).

3.2 Microwave Interaction with Metals

Normally MW frequency is reflected from the metal surface because the depth of penetration of MW is in the order of nanometers. So for a bulk metal there is almost no effect of the MW. But for the thin film metal of nanometer (nm) size has a great impact of MW. As MW can penetrate the metal up to few nanometers to micrometer range.

The distance from the surface into the material at which the power drops to e^{-1} of the original value is known as the depth of penetration or skin depth. In case of bulk metal we can calculate the depth of penetration (δ) for microwave frequency-

$$\delta = \sqrt{\frac{2}{\omega\mu_0\sigma}} \quad (3.1)$$

Where δ is depth of penetration, ω is the angular frequency ($\omega = 2\pi f$, f is the microwave frequency), μ_0 is the free space permeability and σ is the conductivity of the material. We want to calculate the depth of penetration for bulk Au then $\sigma = 43.5 \times 10^6 \Omega^{-1} / m$, assuming $f = 2.45 \text{ GHz}$ and using (3.1) we get $\delta = 1.54 \mu m$. So from the calculation we can see that for a bulk Au metal the depth of penetration is in micrometer range.

Again MW is an electromagnetic wave, so there will be eddy current creation inside the metal film which results heating inside the metal film (Fig. 3.2). It was reported in [67] that after the irradiation of 2.45 GHz MW frequency with 563 W incident flux of the microwave and 34.6 nm & 29.5 nm metal film thicknesses the heat increased inside the metal film very abruptly. Within few seconds the temperature rises up to 550 K and become steady. This result is also shown in Fig. 3.3 [67].

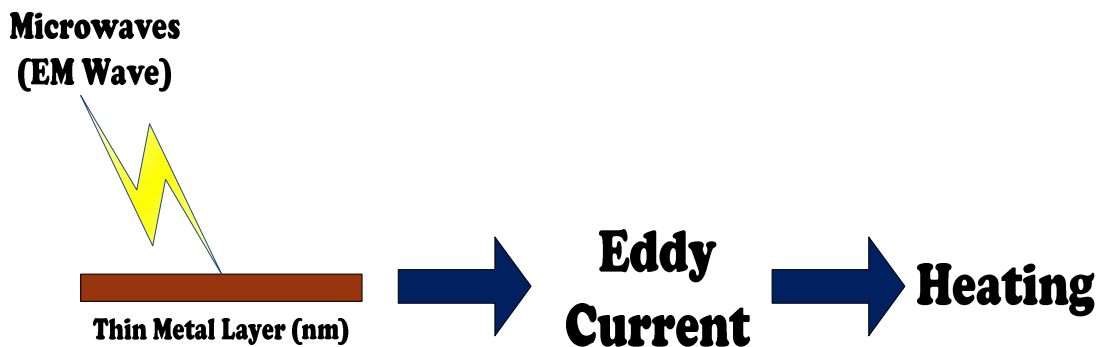


Figure 3.2: Microwave-Metal interaction

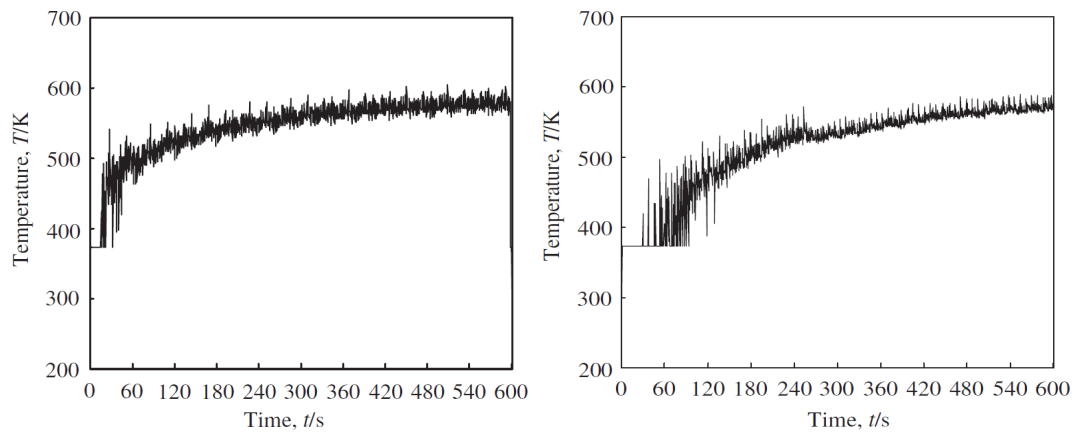


Figure 3.3: Change in temperature of thin Au film with a thickness of 34.6 nm (left figure) and 29.5 nm (right figure) during microwave irradiation [67]

For the SPR based fiber optic sensor normally we use the metal film at the cladding layer to support the surface plasmon wave. And the thickness of this metal film is in nm size so there will be a great effect of the MW on this metal film. In general the metal film used in the fiber sensor for SPR generation is gold (Au) or silver (Ag).

MW is an electromagnetic wave so it has two components; they are H-field and E-field. For the H-field component the heating is much more comparing with the E-field heating. Moreover, one over four times less power is required for heating with MW of H-field than the E-field as reported in [34] as shown in Fig. 3.4.

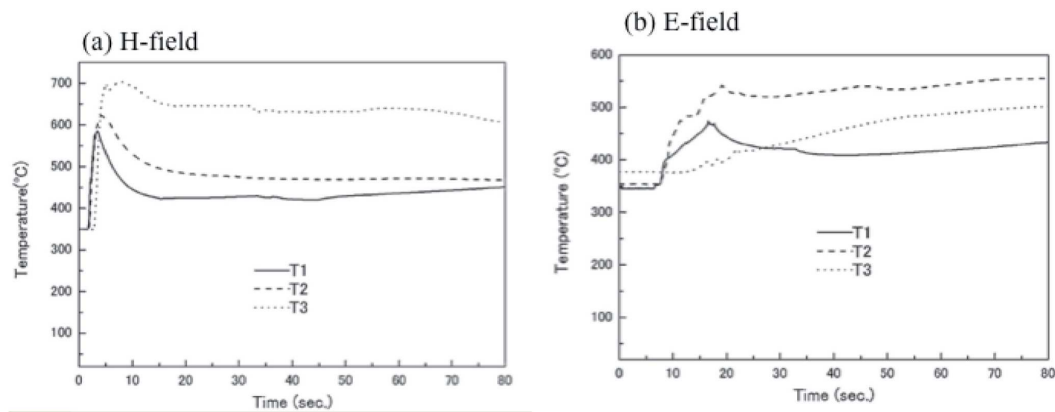


Figure 3.4: Microwave effect on Au film with different thicknesses T1=45 nm, T2=133 nm & T3=407 nm (a) for H-field (b) for E-field [34]

3.3 Microwave Detection Possibility

Natural property of microwaves is that when microwaves impinge on the metal film surface with the thickness of nm size, the temperature of the metal film increases. This temperature change causes the SPR wavelength to shift. Microwave detection flowchart is shown in Fig 3.5 & Fig 3.6. As the temperature is increasing in the metal there will be thermo-optic effect. Due to this thermo-optic effect the effective refractive index and the period of the FBG will be changed. As we already know that the FBG works as per the formula below-

$$m \cdot \lambda_B = 2 \cdot n_{eff} \cdot \Lambda \quad (3.2)$$

In (3.2) there are two parameters (Λ & n_{eff}) that depend on the external change i.e. temperature. Because of the temperature effect the period of the grating and the effective refractive index will change so the Bragg wavelength will shift.

Assume that due to the temperature change the effective index is changing by Δn_{eff} and the period of the grating by $\Delta\Lambda$, which will result in overall Bragg wavelength change $\Delta\lambda_B$. Thus the Bragg condition will take the following form:

$$\begin{aligned} \lambda_B + \Delta\lambda_B &= 2 \cdot (n_{eff} + \Delta n_{eff}) \cdot (\Lambda + \Delta\Lambda) \\ &= 2(n_{eff} \cdot \Lambda + n_{eff} \cdot \Delta\Lambda + \Lambda \cdot \Delta n_{eff} + \Delta n_{eff} \cdot \Delta\Lambda) \end{aligned} \quad (3.3)$$

The last term of the expression can be neglected as it is multiplication of two small quantities. So to express the change of Bragg wavelength (3.2) becomes -

$$\Delta\lambda_B = 2(n_{eff} \cdot \Delta\Lambda + \Lambda \cdot \Delta n_{eff}) \quad (3.4)$$

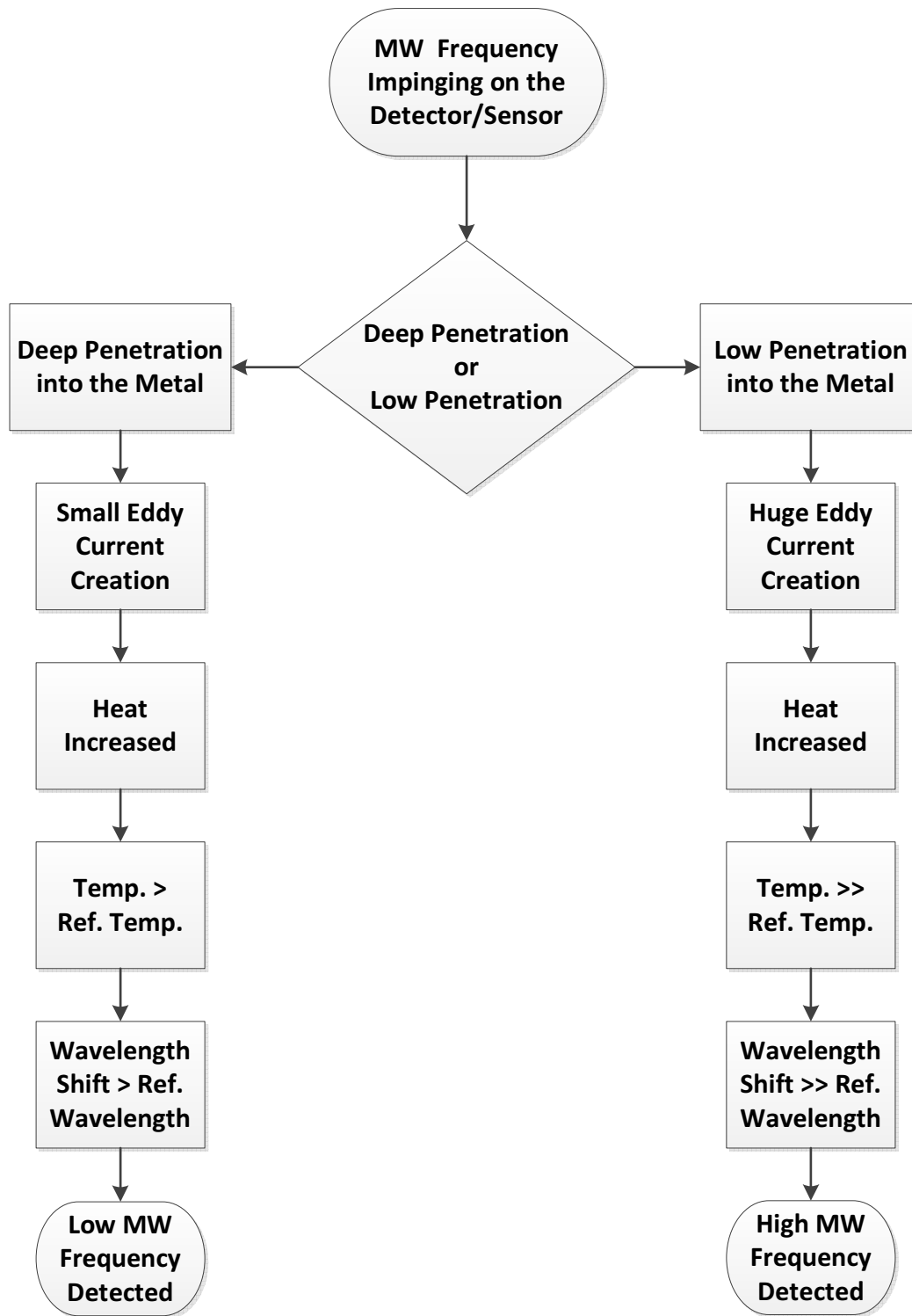


Figure 3.5: Flowchart for the proposed MW detection scheme using Tilted FBG

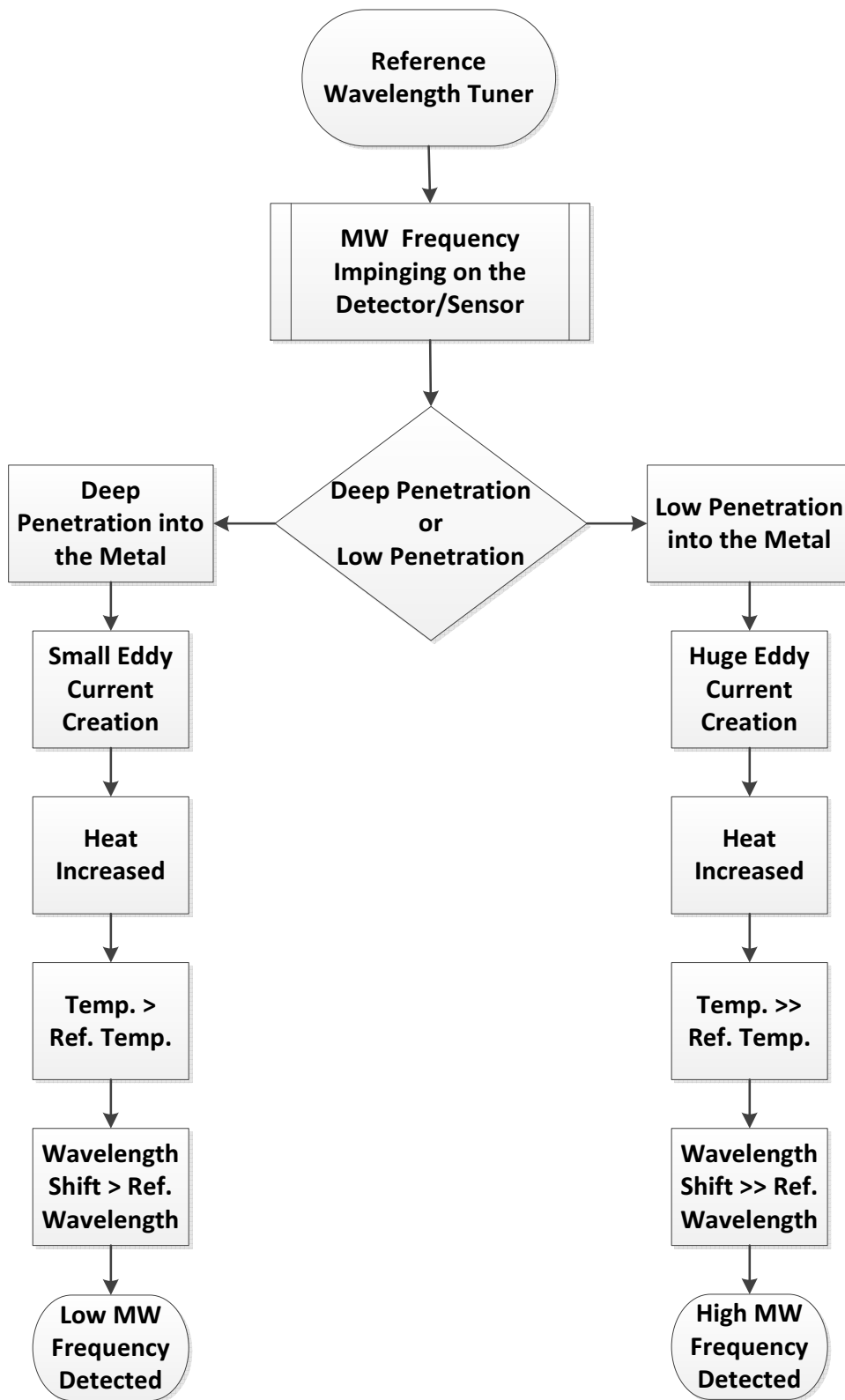


Figure 3.6: Flowchart for the proposed MW detection scheme using Tilted Chirped FBG concept

CHAPTER IV

Experiment & Results

4.1 Experiment for Uniform FBG

A uniform FBG was used in the laboratory to check the temperature effect on the Bragg wavelength. A heating panel was used to heat up the FBG section. The heating panel was connected to a current source so that we can tune the current which results the temperature change of the panel. Input of the fiber was connected to a LASER source and a light coupling arrangement was considered to ensure 100% coupling of the light to the fiber. The output section of the fiber was connected to an Optical Spectrum Analyzer (OSA) thus we can observe the output wave of the FBG. We increased the current from 0 A to 0.80 A as a consequence the temperature change was 24.1 °C to 51 °C. The experimental setup is shown in Fig. 4.1 & Fig. 4.2. The Bragg wavelength shift is listed in the Table 4.1.

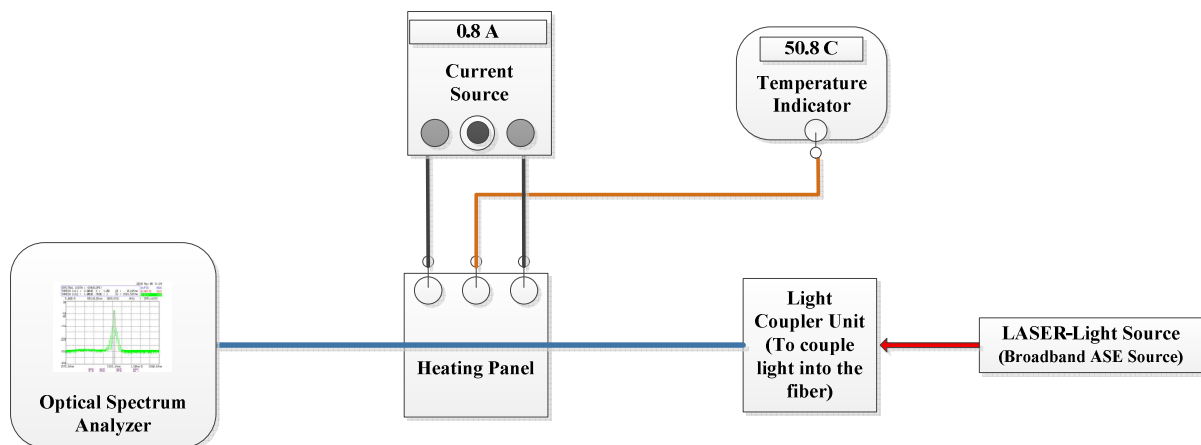


Figure 4.1: Experimental setup

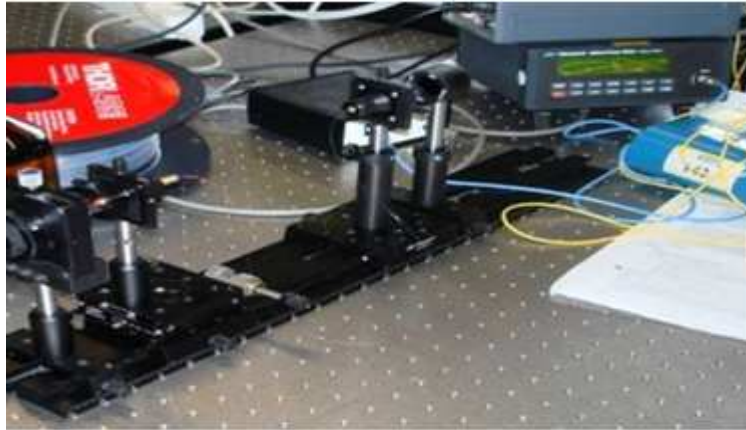


Figure 4.2: Practical work bench

4.2 Experimental Data for Uniform FBG

Table 4.1: Experimental data for uniform FBG

No. of Readings	Current (A)	Temperature (°C)	Wavelength (nm)
1	0.00	24.1	1583.294
2	0.04	24.4	1583.295
3	0.08	25.1	1583.300
4	0.12	25.7	1583.304
5	0.16	26.4	1583.310
6	0.20	27.2	1583.317
7	0.24	28	1583.324
8	0.28	28.8	1583.332
9	0.32	29.7	1583.339
10	0.36	30.8	1583.350
11	0.40	32	1583.359
12	0.44	33.1	1583.370
13	0.48	34.5	1583.383
14	0.52	35.6	1583.392
15	0.56	37.2	1583.408
16	0.60	38.7	1583.422
17	0.64	43.4	1583.471
18	0.78	45	1583.487
19	0.72	47	1583.506
20	0.76	48.8	1583.522
21	0.80	51	1583.544

Experimental result is plotted as Temperature change vs. Bragg wavelength shift (Fig. 4.3) & its linear fitting (Fig. 4.4). One of the observed shifted Bragg wavelength in Optical Spectrum Analyzer (OSA) is shown in Fig. 4.5.

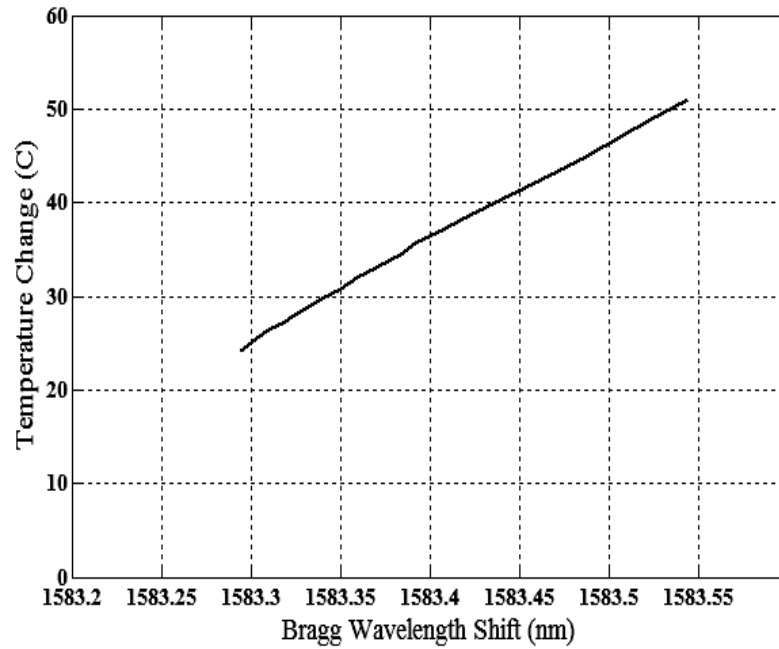


Figure 4.3: Bragg wavelength dependence on temperature.

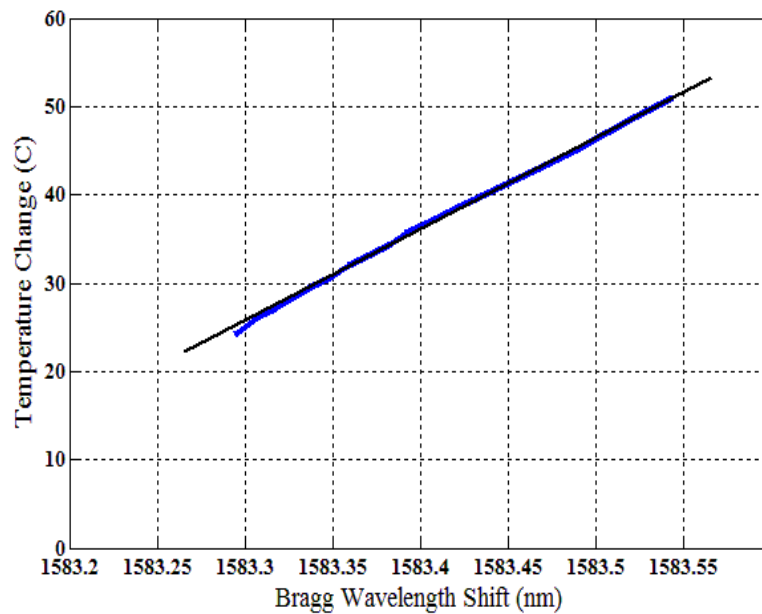


Figure 4.4: Experimental results of the Bragg wavelength dependence on temperature and linear fitting.

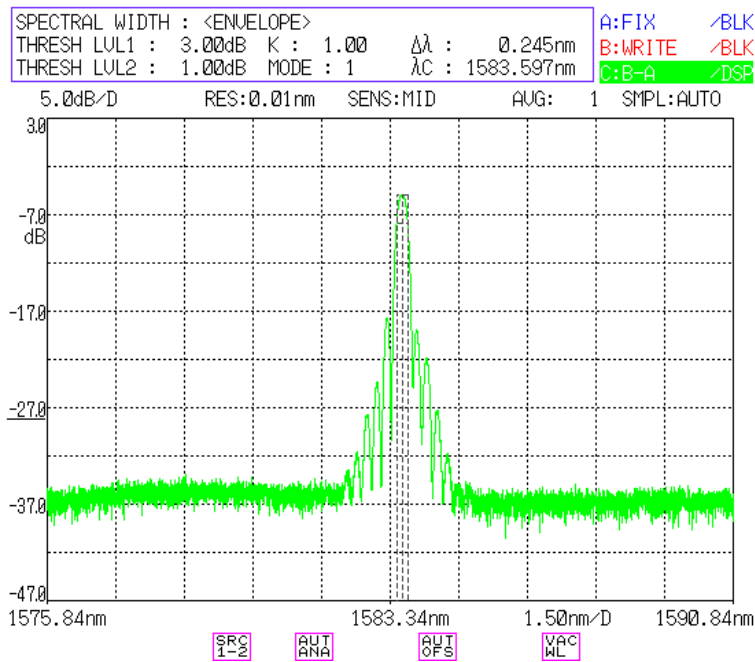


Figure 4.5: Observed Bragg wavelength in Optical Spectrum Analyzer.

4.3 Calculation of Error for Uniform FBG

For the calculation of the error [35] let us consider the measurements with readings 14 and 21.

Table 4.2: Data for error calculation of FBG

No. of Readings	Temperature (°C)	Wavelength (nm)
14	35.6	1583.392
21	51	1583.544

The absolute error of the temperature is 0.1°C and for wavelength 0.001 , so the sensitivity is:

$$\begin{aligned}
 S &= \frac{(\lambda_{21} \pm \Delta\lambda_{err}) - (\lambda_{14} \pm \Delta\lambda_{err})}{(T_{21} \pm \Delta T_{err}) - (T_{14} \pm \Delta T_{err})} = \frac{(\lambda_{21} - \lambda_{14}) \pm \Delta\lambda_{dif_err}}{(T_{21} - T_{14}) \pm \Delta T_{dif_err}} \\
 &= \frac{0.152}{15.4} \pm \Delta S_{err} = 0.0099 \pm \Delta S_{err}
 \end{aligned} \tag{4.1}$$

Where the errors from the difference can be calculated from absolute errors by:

$$\begin{aligned}\Delta\lambda_{dif_err} &= \sqrt{(\Delta\lambda_{err})^2 + (\Delta\lambda_{err})^2} = \sqrt{2(\Delta\lambda_{err})^2} \\ &= \sqrt{2(0.001)^2} = 0.0014\end{aligned}\quad (4.2)$$

$$\begin{aligned}\Delta T_{dif_err} &= \sqrt{(\Delta T_{err})^2 + (\Delta T_{err})^2} = \sqrt{2(\Delta T_{err})^2} \\ &= \sqrt{2(0.1)^2} = 0.14\end{aligned}\quad (4.3)$$

Error generated from the ratio can be calculated in the following way:

$$\begin{aligned}\Delta S_{err} &= S \cdot \sqrt{\left(\frac{\Delta\lambda_{dif_err}}{\Delta\lambda}\right)^2 + \left(\frac{\Delta T_{dif_err}}{\Delta T}\right)^2} \\ &= 0.0099 \cdot \sqrt{\left(\frac{0.0014}{0.152}\right)^2 + \left(\frac{0.14}{15.4}\right)^2} = 0.00013nm/^{\circ}C \\ \Delta S_{err} &= 0.13 pm/^{\circ}C\end{aligned}\quad (4.4)$$

So the sensitivity with the calculated error is: $(9.9 \pm 0.13) pm/^{\circ}C$

4.4 Experiment for Chirped Fiber Bragg Grating

In a similar way we conducted a common experiment on CFBG to know the exact temperature effect on it. The experimental setup was same as before. It is mentioned before that in (3.2) two parameters depend on external condition change, i.e. change of temperature. These parameters are- effective index of the core (n_{eff}) and the period of the grating (Λ). When temperature changes the effective index is also changed due to thermo-optic effect, while the period changes due to thermal expansion of the glass. As a result of temperature variation the effective index is changing by Δn_{eff} and the period of the grating by $\Delta\Lambda$, which will result in overall Bragg wavelength change $\Delta\lambda_B$.

A current source to heat the panel was used (as we did previously) where the CFBG was attached. The current was increased from 0A to 0.8A which results the temperature increase of the panel from $27.7^{\circ}C$ to $54.6^{\circ}C$ respectively. Due to the temperature change the related wavelength shift is listed in Table 4.3. This result is plotted in Fig. 4.6.

4.5 Experimental Data for Chirped FBG

Table 4.3. Experimental data for CFBG

No. of Readings	Current (A)	Temperature (°C)	Wavelength (nm)
1	0.00	27.7	1583.310
2	0.04	28.4	1583.312
3	0.16	30.7	1583.313
4	0.20	31.6	1583.318
5	0.24	32.5	1583.322
6	0.28	33.4	1583.327
7	0.32	34.5	1583.334
8	0.36	35.7	1583.342
9	0.40	37.0	1583.351
10	0.44	38.5	1583.361
11	0.48	40.1	1583.374
12	0.52	41.5	1583.385
13	0.56	43.2	1583.399
14	0.60	44.7	1583.414
15	0.64	46.8	1583.433
16	0.78	48.8	1583.450
17	0.76	52.6	1583.486
18	0.80	54.6	1583.502

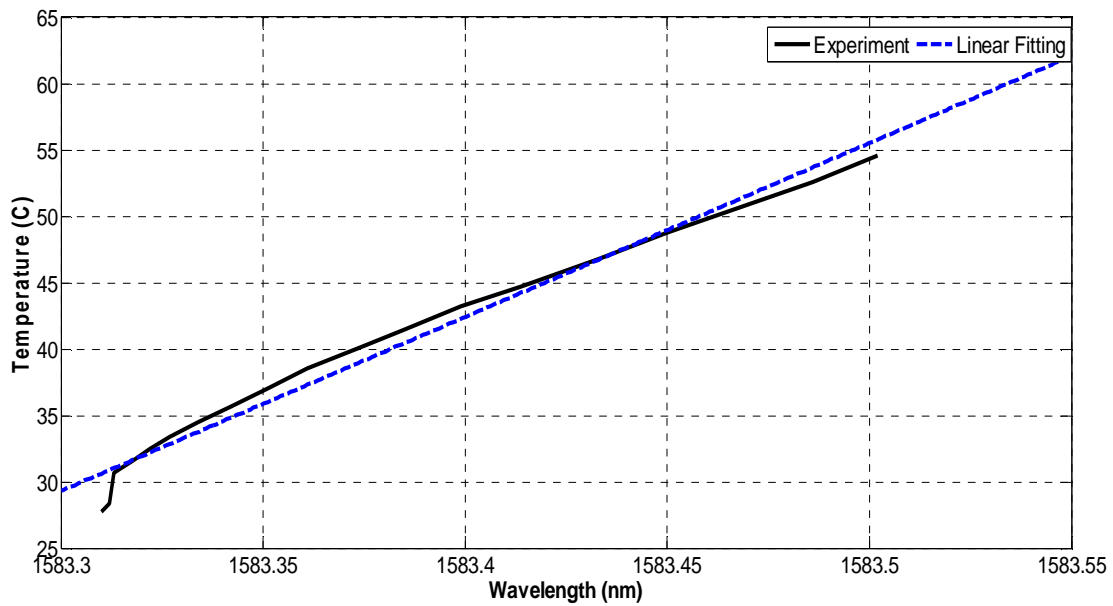


Figure 4.6: Bragg wavelength dependence on temperature and linear fitting for CFBG

In Fig. 4.6, linear fitting is performed by MATLAB and is presented together with experimentally obtained curve of Bragg wavelength dependence on temperature. The sensitivity according to this fitting is $7.44\text{pm}/^{\circ}\text{C}$.

If we pay more attention to the experimental curve, we can see that in the beginning, the measurement weren't performed appropriately, as in this region the dependence is not linear. Additionally, the linear region is started from the temperature of 42°C and finished at 55°C . The result of sensitivity was calculated only for that region and found as $8.9\text{pm}/^{\circ}\text{C}$.

From the above result it is clear that the temperature response for the CFBG is linear same as the uniform FBG for a specific wavelength. From the experimental result we can see that there is an average 6 pm wavelength shift due to 1°C temperature change.

4.6 Calculation of Error for Chirped FBG

As we did previously, for the calculation of error let us consider the No. of readings 12 and 18.

Table 4.4: Data for error calculation of CFBG

No. of Readings	Temperature (°C)	Wavelength (nm)
12	41.5	1583.385
18	54.6	1583.502

The absolute error of the temperature is 0.1 °C and for wavelength 0.001, so the sensitivity is:

$$\begin{aligned}
 S &= \frac{(\lambda_{18} \pm \Delta\lambda_{err}) - (\lambda_{12} \pm \Delta\lambda_{err})}{(T_{18} \pm \Delta T_{err}) - (T_{12} \pm \Delta T_{err})} \\
 &= \frac{(\lambda_{18} - \lambda_{12}) \pm \Delta\lambda_{dif_err}}{(T_{18} - T_{12}) \pm \Delta T_{dif_err}} = \frac{0.117}{13.1} + \Delta S_{err} \\
 &= 0.0089 + \Delta S_{err}
 \end{aligned} \tag{4.5}$$

Where, the errors from the difference can be calculated from absolute errors by:

$$\begin{aligned}
 \Delta\lambda_{dif_err} &= \sqrt{(\Delta\lambda_{err})^2 + (\Delta\lambda_{err})^2} \\
 &= \sqrt{2(\Delta\lambda_{err})^2} = \sqrt{2(0.001)^2} = 0.0014
 \end{aligned} \tag{4.6}$$

$$\begin{aligned}
 \Delta T_{dif_err} &= \sqrt{(\Delta T_{err})^2 + (\Delta T_{err})^2} \\
 &= \sqrt{2(\Delta T_{err})^2} = \sqrt{2(0.1)^2} = 0.14
 \end{aligned} \tag{4.7}$$

The error coming from the ratio can be calculated in the following way:

$$\begin{aligned}
 \Delta S_{err} &= S \cdot \sqrt{\left(\frac{\Delta\lambda_{dif_err}}{\Delta\lambda}\right)^2 + \left(\frac{\Delta T_{dif_err}}{\Delta T}\right)^2} \\
 &= 0.0089 \cdot \sqrt{\left(\frac{0.0014}{0.117}\right)^2 + \left(\frac{0.14}{13.1}\right)^2} \\
 &= 0.0089 \cdot 0.016 = 0.00014 \text{ nm/}^\circ\text{C}
 \end{aligned} \tag{4.8}$$

$$\Delta S_{err} = 0.14 \text{ pm/}^\circ\text{C} \tag{4.9}$$

So the sensitivity of the sensor with the calculated error is: $(8.9 \pm 0.14) \text{ pm/}^\circ\text{C}$.

CHAPTER V

Discussion

From our experiment we can see that there is a linear relationship between the temperature change and the Bragg wavelength shift. It is observed from the experimental data that the average Bragg wavelength shift is 0.009 nm per degree C. This implies that with the change of temperature the Bragg wavelength shifts linearly. As reported in [36] they got the result shown in Fig. 5.1.

If we compare these two results we can see the linearity. In a similar way in case of Tilted FBG, the Bragg wavelength shifts due to the temperature change. So the SPR based TFBG sensor can sense a small temperature change from the SPR wavelength shift observation.

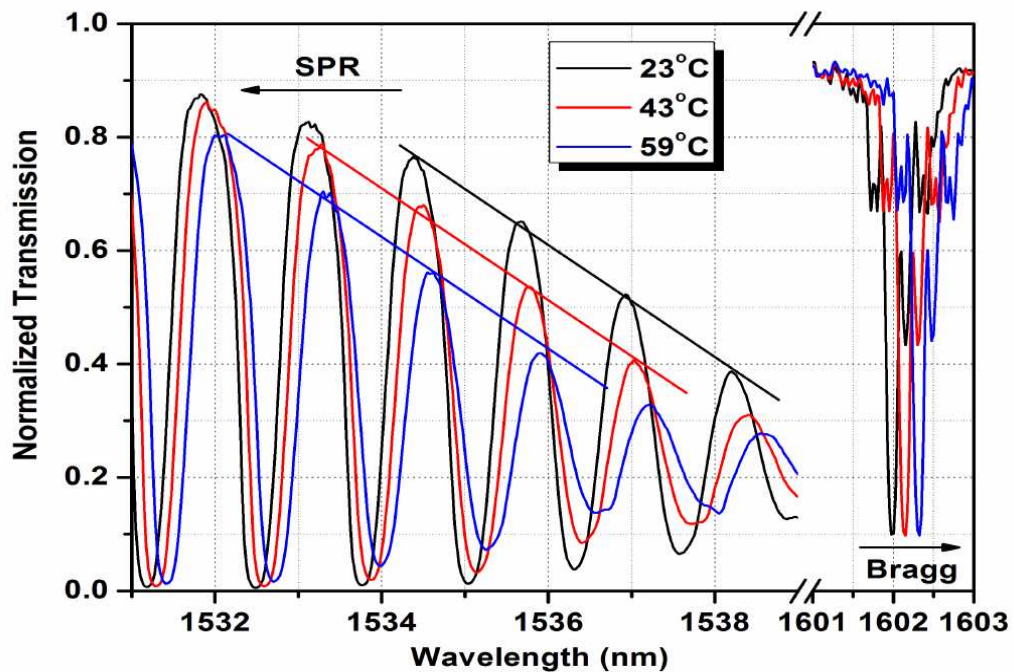


Figure 5.1: SPR and Bragg wavelength shift due to temperature change (Reprinted with permission-[36]).

When a MW is impinging on the metal film of this kind of sensor then the temperature of the metal film will be increased. The corresponding temperature change can be identified by measuring the SPR wavelength shift. As the penetration depths of various MW frequencies are different, the observed wavelength shift will also be different. By comparing the wavelength shift of the SPR wave with the reference wave (at room temperature) we can detect different MW frequencies.

If the MW frequency is higher, it cannot penetrate deeply into the metal but the eddy current will be increased and it will produce much more heat. As a consequence the wavelength shift will be greater from the reference wavelength. And for lower MW frequency, penetration will be higher but the eddy current will be lower compared with the higher MW so temperature will be increased from the reference temperature, wavelength will shift from the reference wavelength but not that much as it is for high MW frequency (referring to the flowcharts in chapter-3). So it is possible to detect the MW frequency by using the SPR based TFBG sensor with a small modification. The proposed sensor is shown in Fig.

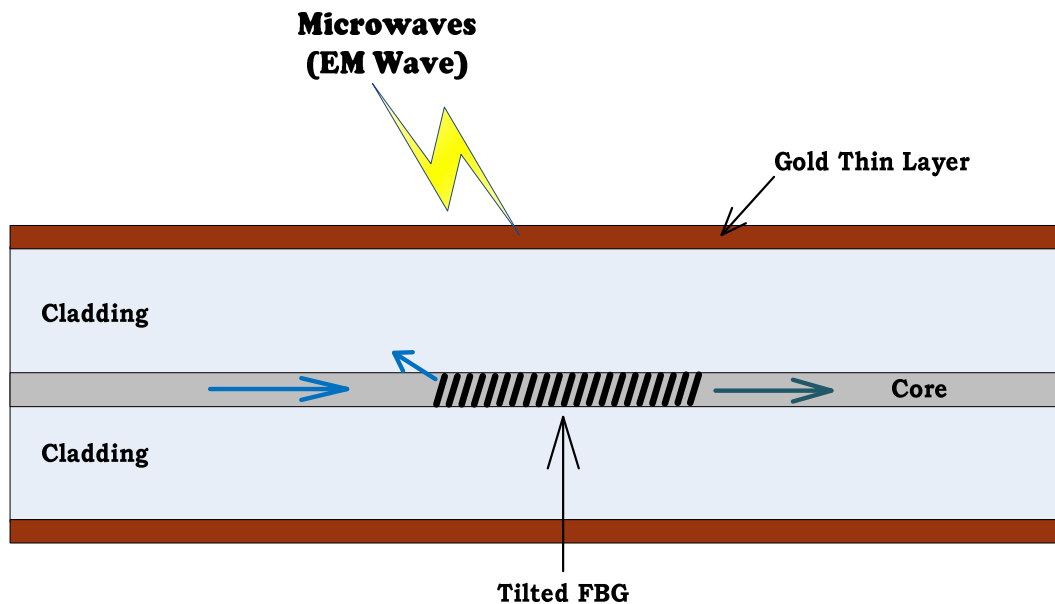


Figure 5.2: Proposed MW sensor using TFBG

The thickness of the metal film has great importance to sense the MW frequency. It is explained in chapter six. The penetration depth of MW frequency varies with the corresponding frequency change (higher or lower MW frequency). If we vary the thickness of the metal layer then the sensitivity of the sensor will be changed as the SPR is changing. If we use the thickness of the metal around 60 nm then it is possible to achieve large refractive index change as well as large range of resonance wavelengths as reported in [37]. So the sensitivity range of the sensor is increased. But it is necessary to design the sensor in an optimized way because the MW penetration rate is not too much for metals due to the attenuation in the metal. It was measured for K-band MW frequency by Maxwell that the attenuation in gold is 0.6 dB/meter and in Silver it is 0.41 to 0.57 dB/meter as reported in [38].

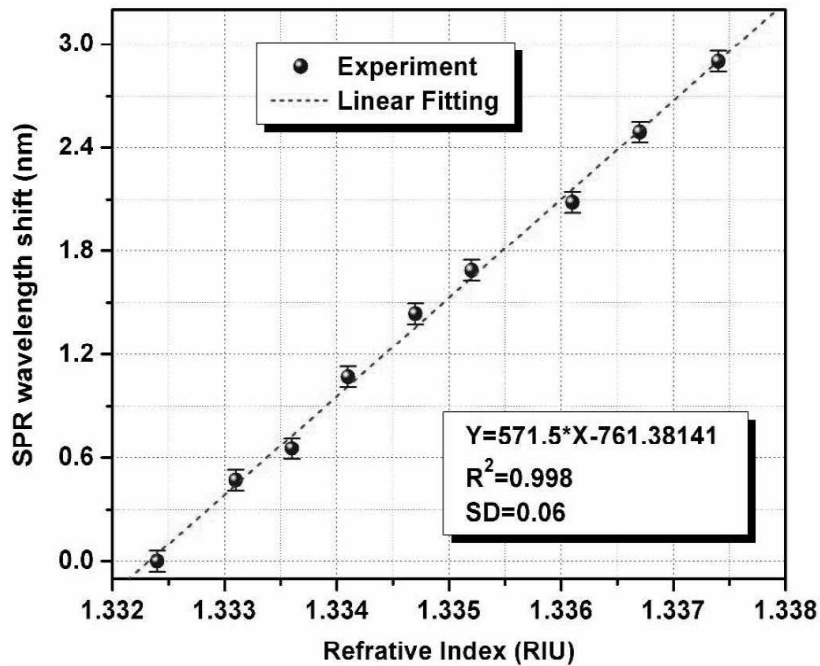


Figure 5.3: SPR wavelength shift corresponding to the refractive index change (Reprinted with permission-[36])

For example if we consider the Fig. 5.3 we can see that the SPR based TFBG sensor can sense a small temperature change (which is related to the refractive index change) from the SPR wavelength shift observation. So when a MW is impinging on the metal film of this kind of sensor then the temperature of the metal film will be increased. The corresponding temperature change can be measured by measuring the SPR wavelength shift. By comparing the wavelength shift of the SPR wave with the reference we can detect the MW frequency. So it is possible to detect the MW frequency by using the SPR based TFBG sensor.

CHAPTER VI

Analysis

It is clear from the discussion that the thickness of the metal film has great importance to sense the MW frequency. The penetration depth of MW frequency varies with the corresponding frequency change (higher or lower MW frequency). If we vary the thickness of the metal layer then the sensitivity will also vary.

For different microwave frequency the depth of penetration into the metal will be different. Considering the Au metal film with conductivity of $20 \times 10^6 \Omega^{-1}/\text{m}$ (thickness, 55 nm [69],[70]) and using (3.1) the depth of penetration into the metal film is calculated in Table 6.1.

Table 6.1. Microwave frequency and Depth of penetration

Sl. No.	MW frequency (GHz)	Conductivity (for thin Au film)	Depth of penetration (nm)
1	300	$20 \times 10^6 \Omega^{-1}/\text{m}$	205.5
2	200		251.8
3	100		356
4	50		503.5
5	40		563
6	30		650
7	20		796
8	15		919
9	10		1126
10	5		1592
11	4		1780
12	2.45		2275
13	1.9		2583
14	1.8		2654
15	0.9		3753
16	0.85		3862
17	0.3		6500

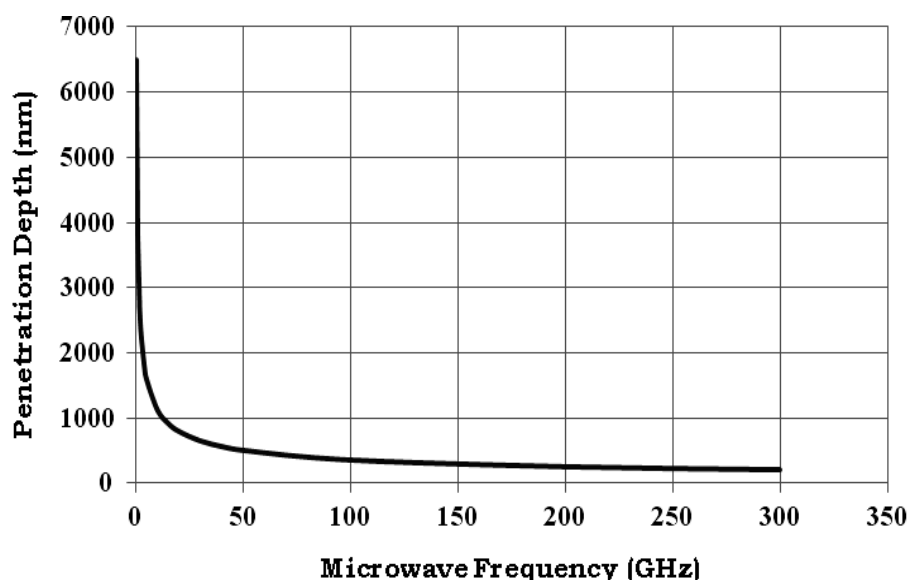


Figure 6.1: Microwave frequency vs penetration depth for Au metal film

It is clear from Fig. 6.1 that for lower microwave frequency the penetration depth is higher and for higher microwave frequency the penetration depth is lower. Though the penetration depth for higher microwave frequency is lower but the eddy current creation in the metal is high for high microwave frequency and vice versa.

It is reported in [40] the Au thickness affects the SPR. When the thickness of the Au film is 60 nm to 70 nm the SPR wavelength shifts from 608 nm to 765 nm with respect to the refractive index change from 1.33 to 1.40. When the thickness is decreasing the SPR wavelength shift is also decreasing. As example at 20 nm film thickness the SPR wavelength shifts from 560 nm to 620 nm.

So, if we vary the thickness of the metal layer then the sensitivity of the sensor is also changed as the SPR is changing. When the thickness of the metal is around 60 nm, it is possible to achieve large refractive index change as well as large range of resonance wavelengths. More over the thickness of the metal will also affect the transmitted light as well [40].

The quality factor of the sensor is also dependent on the thickness of the metal film as reported in [39]. It was experimentally shown that gold film thickness is also responsible for the quality factor. In this experiment they used the 820 nm reflectance wavelength. They found a good quality factor for the Au film thickness ranging from 60 nm to 75 nm. SPR spectrum will be sharper if the quality factor is higher and sharp SPR spectrum is desirable for sensing application. It was measured that at 64 nm gold thickness, the SPR spectrum can get highest quality factor.

It is also possible to use metal alloy to achieve SPR rather than the single metal (like only Au or Ag). It was reported in [42] that the sensitivity and the signal to noise ratio (SNR) for Au-Ag alloy film is better than the conventional single metal layer.

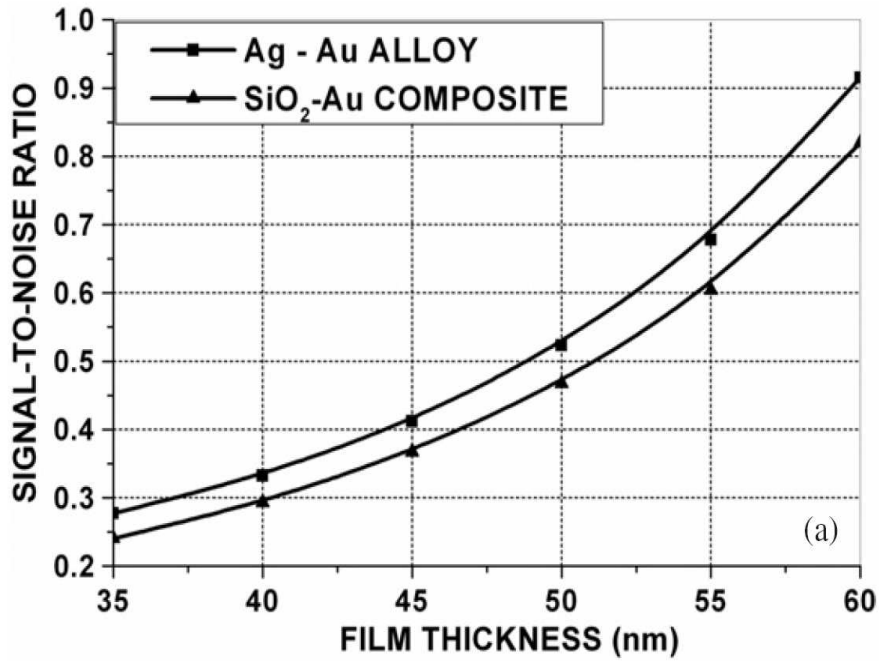


Figure 6.2: SNR vs. Ag-Au alloy film thickness (Reprinted with permission-[42])

From the Fig. 6.2 we can see that the SNR is higher for Ag-Au alloy film than the SNR for single metal or SiO_2 - Au composite. For the alloy the SNR goes from 0.28 to 0.92 and for the single layer metal it goes from 0.24 to 0.82.

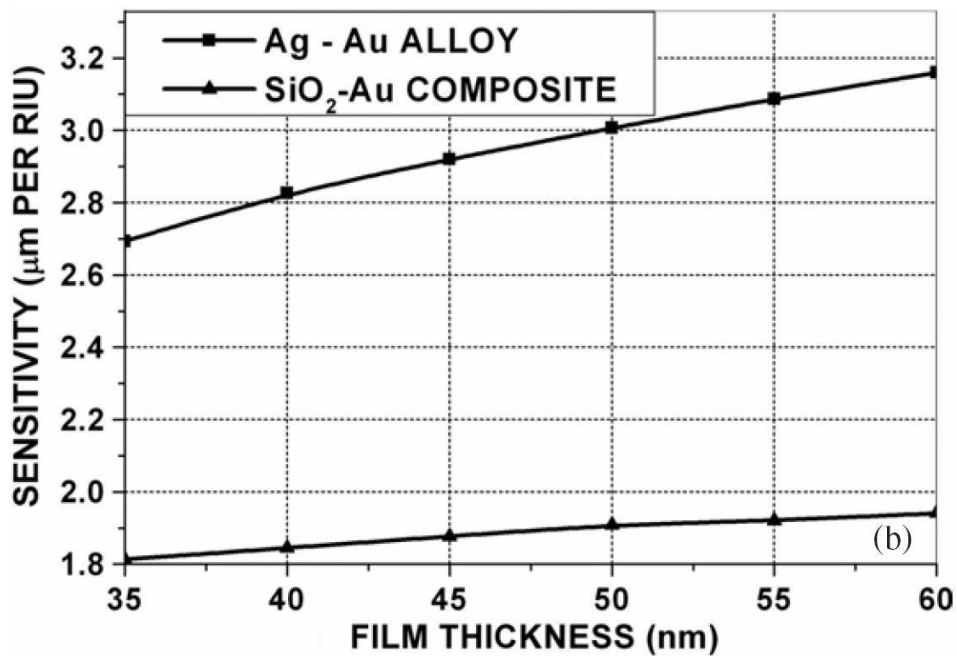


Figure 6.3: Sensitivity vs. Ag-Au alloy film thickness (Reprinted with permission-[42])

Similarly considering Fig. 6.3 it is observed that the sensitivity is higher for Ag-Au alloy film than the sensitivity for single metal or SiO_2 - Au composite. For the alloy the sensitivity range from 2.65 μm per RIU to 3.18 μm per RIU for the thickness of the metal film from 35 nm to 60 nm. Whereas the sensitivity range for single metal film is from 1.80 μm per RIU to 1.88 μm per RIU.

For this Ag-Au alloy film we have to consider some facts that's related to the performance of the sensor like [42]-

To get good SNR and sensitivity we have to use high concentration of the Ag in the alloy comparing with the Au concentration. The sizes of the Ag and Au nanoparticle in the alloy should also be considered to get better performances. Finally we have to use the alloy thickness in an optimized way to get good performance from the sensor.

As reported in [40] that Au-Cr composite can be used for the SPR generation by forming the Kretschmann configuration on the fiber cladding.

It was also reported that the metallic coating on the fiber for SPR generation can also be done by using Indium Tin Oxide (ITO) which can be used in sensing application [43].

Moreover, instead of using SPR-TFBG sensor we can use different configuration as reported in [40]-

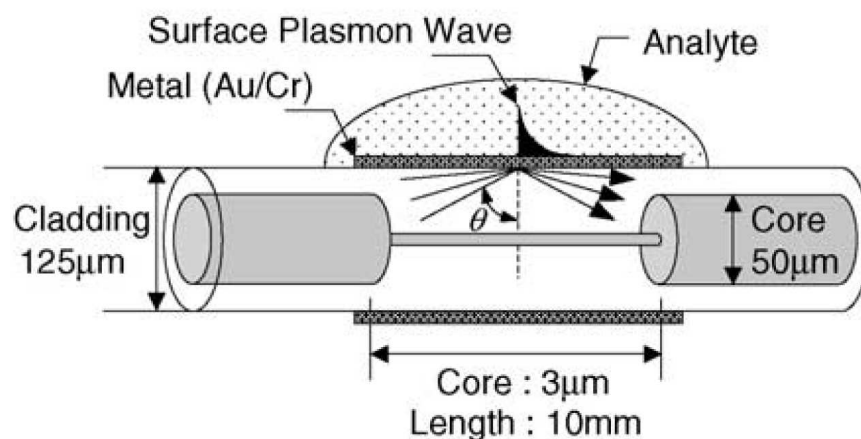


Figure 6.4: SPR based Hetero-core structured optical fiber sensor [40]

As shown in the Fig. 6.4 that there are two kinds of fibers one is transmission fiber with large diameter and other is thin diameter fiber which inserted into the transmission fiber. This thin diameter fiber works as the sensing region. And the Cr-Au is deposited around this region for SPR generation. When the light reaches at the end of the transmission fiber and at the beginning of the thin diameter or core fiber then most of the light wave becomes leaky modes and evanescent SPW

is generated. Here the Cr is used in between the Au and cladding for firm adhesion which is similar as Kretschmann configuration [40].

There is another possible configuration that can be used to get SPR if the propagation constant can be matched. As we know that if we bend the optical fiber, when it exceeds certain radius the guided modes become cladding modes. This is only possible when the bend reaches at certain radius. Here we will find out the exact radius at which the guided modes become cladding mode. The proposed configuration is shown in Fig. 6.5.

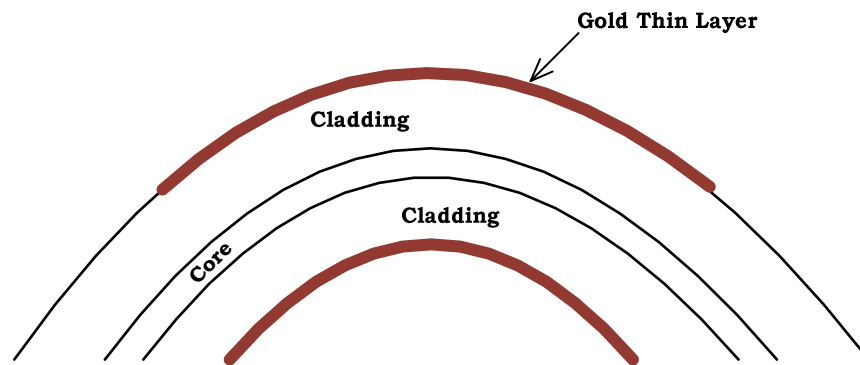


Figure 6.5: Bended waveguide with fixed radius and thin gold layer

We will be considering the waveguide (WG) bending effect for Silicon on Insulator (SOI) and Silica on Silicon (SOS) material system. To generalize the analysis, specific polarization issue was not considered here.

6.1 Waveguide with SOI Material System

A mode is guided when the modulus of the effective index is larger than the modulus of the refractive index of the cladding, in this case when $|n_{\text{eff},2}| > |n_{\text{eff},1}|$. We calculated the effective index by using effective index method (assuming common parameters):

$$n_{\text{eff},1} = 2.517287, \quad n_{\text{eff},2} = 2.822689$$

From the simulation (using CAD tools i.e. *Python*, *Maple*) we see that the first order mode becomes guided at WG width of about $0.60 \mu\text{m}$ which is shown in Fig. 6.6.

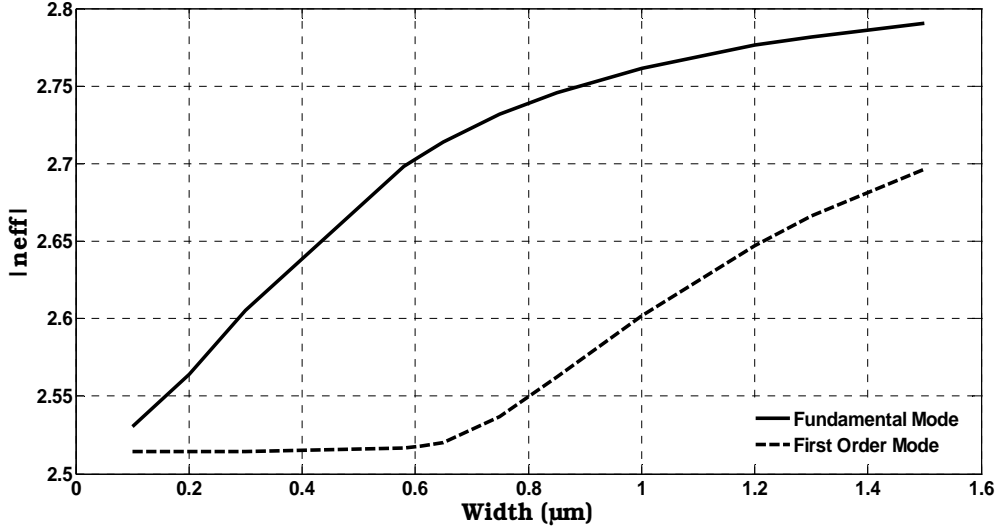


Figure 6.6: n_{eff} of different modes as a function of the WG width for SOI

We calculated the optimal width of the waveguide, at which a second mode starts to propagate theoretically. The optimal width can be calculated as-

$$d = \frac{\lambda}{2} \cdot \frac{1}{\sqrt{n_{\text{eff},2}^2 - n_{\text{eff},1}^2}} = 0.61 \mu\text{m} \quad (6.1)$$

Which corresponds to the value derived from the simulation results and is listed in Table 6.2.

Table 6.2: Effective index of the fundamental and first order mode as a function of WG width for SOI

Width (μm)	n_{eff} , Fundamental Mode	n_{eff} , First Order Mode
0.1	$2.530534 + 0.000018j$	$2.514119 - 0.000207j$
0.2	2.563973	$2.514266 - 0.000193j$
0.3	2.605265	$2.514449 - 0.000176j$
0.58	2.698217	$2.516418 - 0.000035j$
0.61	2.705179	$2.517420 + 0.000004j$
0.65	2.713694	$2.520073 + 0.000041j$
0.75	2.731649	$2.537011 + 0.000006j$
0.85	2.745759	2.562238
1.0	2.761698	2.601892
1.2	2.776416	2.647381
1.3	2.781886	2.666058
1.5	2.790304	2.696294

6.1.1 Eigenmodes of SOI Bent Waveguide

The n_{eff} of a circular bent waveguide was calculated as a function of the radius of the bend. We determined the values for the *start*, *end* & *steps* parameter using *Maple*. The number of steps was chosen so that there are 15 steps (or more) inside the waveguide. The contrast between the refractive index of the waveguide and the index of the cladding should be clearly visible so the mode will be confined in the waveguide, this means that we can't choose the *start* and *end* values too far apart. However, we also need to leave some of the cladding area (with a higher refractive index) in the simulation, because the program (simulator) uses this area to determine the losses.

We expect the profile of the guided mode to be concentrated in the outer rim of the bent waveguide, because the mode is most strongly guided in the area with the highest refractive index. When the radius becomes smaller, the mode will shift even more towards the outer edge of the waveguide. As the refractive index will be larger than the effective index of the waveguide mode at a certain distance from the bend, the effective index of a waveguide bend mode will be complex.

After choosing the correct values for the parameters, we obtained n_{eff} as a function of the radius of the bend. From n_{eff} the attenuation coefficient α_{φ} can be calculated through the formula-

$$\alpha_{\varphi} = -\text{Im}(n_{\text{eff}}) \cdot k_0 \cdot R \quad (6.2)$$

Where R- radius, n_{eff} - effective index and $k_0 = 2\pi/\lambda$. This formula also shows that when we are looking for a guided mode (with low losses), we need to find the mode that has the lowest imaginary index.

The losses in dB/90° can be calculated by using-

$$\text{Loss}[\text{dB}/90^{\circ}] = -10 \cdot \log\left(e^{-\alpha_{\varphi} \frac{\pi}{2}}\right) = 10 \cdot \alpha_{\varphi} \cdot \frac{\pi}{2} \cdot \log(e) \quad (6.3)$$

The values of n_{eff} , α_{φ} and the loss as a function of the radius are given in Table 6.3. The losses versus radius are graphically represented in Fig. 6.7 and Fig. 6.8 describes the relation between effective index and radius of the waveguide bend. If we accept losses of up to 2dB/90°, the minimum radius of the bend is 8 μm for SOI system. Small bends can be made because of the high refractive index contrast between the core and the cladding.

Table 6.3: Effective index and loss as a function of the radius of the bend for SOI

Radius (μm)	$\text{Re}(n_{\text{eff}})$	$\text{Im}(n_{\text{eff}})$	$ n_{\text{eff}} $	α_{φ}	Loss [db/90°]
40	2.718803	0	2.718803	0	0
30	2.733720	-0.000005	2.733720	0.0006081	0.0041480
20	2.747102	-0.000131	2.747102	0.0106206	0.0724525
15	2.770437	-0.000679	2.770437	0.0412866	0.2816524
10	2.800504	-0.004459	2.800507	0.1807531	1.2330760
05	2.926480	-0.028697	2.926621	0.5816405	3.9678830

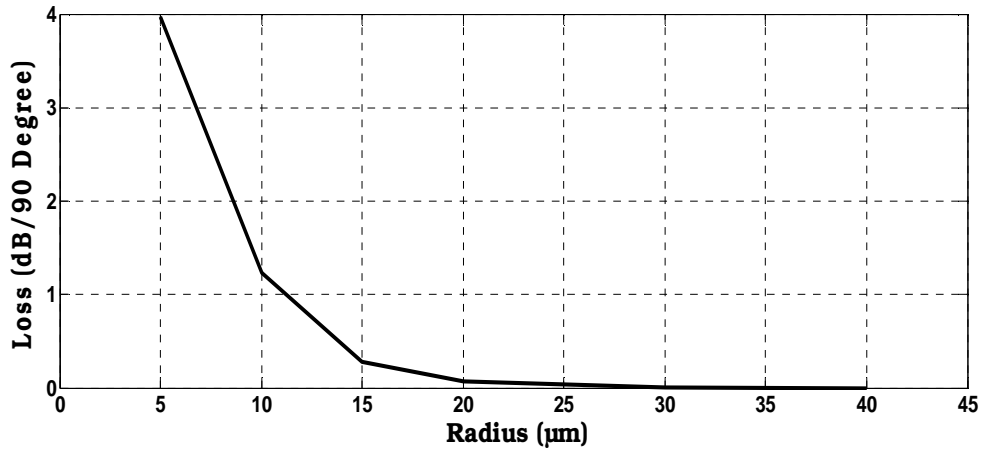


Figure 6.7: Losses as a function of the radius for the WG bend in case of SOI

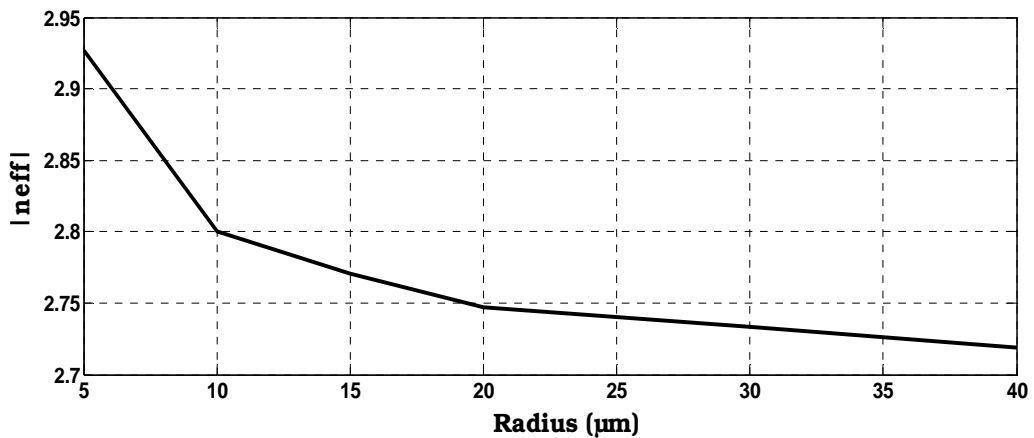


Figure 6.8: n_{eff} as a function of the radius of the WG bend in case of SOI

6.2 Waveguide with SOS Material System

In case of the SOS waveguide we obtained the effective index in a similar manner as it was calculated for SOI system, which are: $n_{\text{eff},1} = 1.45$, $n_{\text{eff},2} = 1.457476$.

From the simulation results for this system we see that the first order mode is guided from a width of $5.26 \mu\text{m}$ (referring to the Fig. 6.9). When we use (6.1) as we did for SOI, we got the theoretical value of the optimal width which was $5.26 \mu\text{m}$, this corresponds to the value derived from the simulation results and are given in Table 6.4.

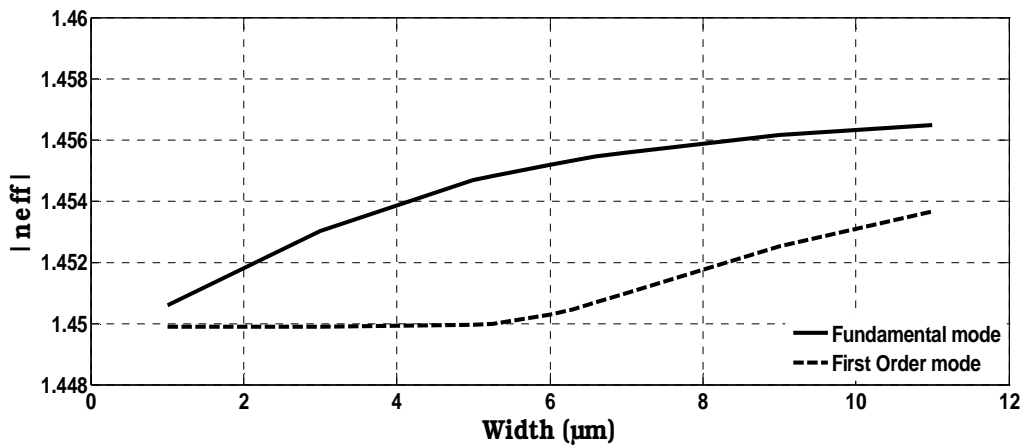


Figure 6.9: n_{eff} of the different modes as a function of the width for SOS

Table 6.4: Effective index of the fundamental and first order mode as a function of WG width for SOS

Width (μm)	n_{eff} Fundamental Mode	n_{eff} First Order Mode
1	1.450591	1.449877 -0.000001j
3	1.453017	1.449894 -0.000001j
5	1.454671	1.449965
5.26	1.454824	1.450000
6	1.455199	1.450271
6.3	1.455330	1.450464
6.6	1.455451	1.450683
7	1.455597	1.450997
9	1.456141	1.452509
11	1.456481	1.453659

6.2.1 Eigenmodes of SOS Bent Waveguide

Following the same simulation (with different parameters) as we conducted for SOI system we got the values of n_{eff} , α_ϕ and the loss as a function of the radius for SOS system. These results are listed in Table 6.5. The losses are graphically represented in Fig. 6.10 as a function of radius. The effect of radius with effective index is also shown in Fig. 6.11. If we accept losses of up to $2\text{dB}/90^\circ$ as we considered for SOI, the minimum radius of the bend is 2.5 mm for SOS system. Smaller bends cannot be made because of the low refractive index contrast between the core and the cladding.

Table 6.5: Effective index and loss as a function of the radius of the band for SOS

Radius (μm)	$\text{Re}(n_{\text{eff}})$	$\text{Im}(n_{\text{eff}})$	$ n_{\text{eff}} $	α_ϕ	Loss [db/90°]
1700	1.457722	-0.000220	1.457722	1.516072	10.342463
1750	1.457646	-0.000145	1.457646	1.028618	7.017112
2000	1.457310	-0.000074	1.457310	0.599943	4.092739
2500	1.456758	-0.000032	1.456758	0.324293	2.212291
3000	1.456396	-0.000014	1.456396	0.170254	1.161453
3500	1.456150	-0.000002	1.456150	0.028376	0.193576
4500	1.455842	0	1.455842	0.000000	0.000000

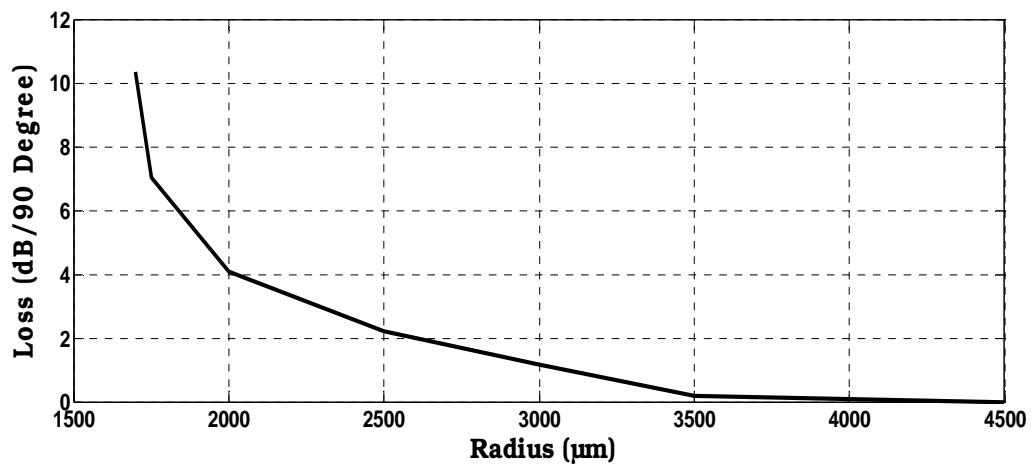


Figure 6.10: Losses as a function of the radius for the WG bend in case of SOS

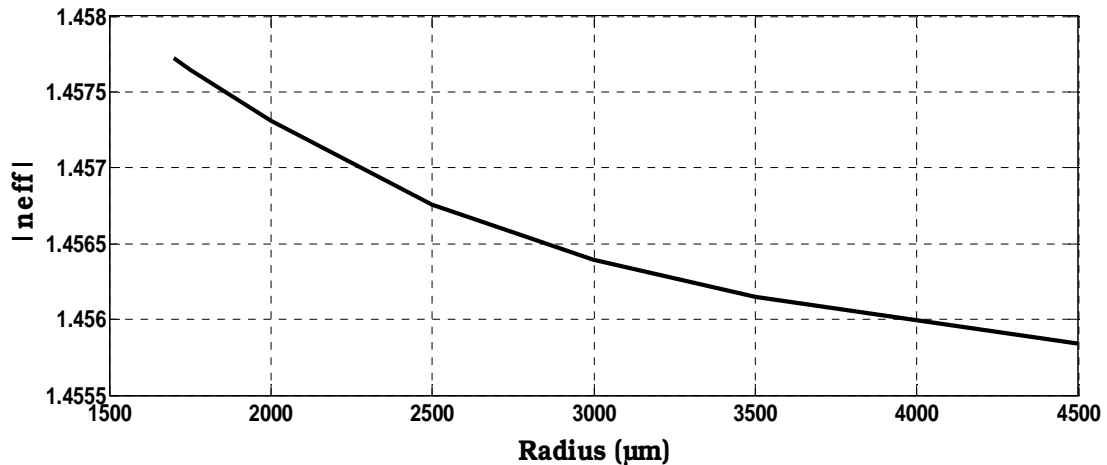


Figure 6.11: n_{eff} as a function of the radius of the WG bend in case of SOS

In this analysis we considered the waveguide bend of 90° . Here the reference acceptable loss we considered is $2 \text{ dB}/90^\circ$. It is clear from the simulation results that in case of SOI waveguide, this acceptable loss was obtained with $8 \mu\text{m}$ bending radius. Whereas for SOS the bend radius was 2.5 mm . Radiation losses increase nearly exponentially with decreasing bend radius. For SOI system the small bend can be obtained due to the high refractive index contrast between the core and cladding but it is not possible for SOS system because of low refractive index contrast between the core and the cladding.

So we can say that in case of SOI material system waveguide, we will get the cladding mode after exceeding the bend radius of $8 \mu\text{m}$ and for SOS material system it is 2.5 mm .

Another important parameter we have to consider for the design for SPR based fiber optic sensor that is the polarization effect. The surface plasmon waves are very much dependent on the polarization effect. So polarization controlling elements are necessary to control the polarization effect on SPR. As a solution of this problem recently new type of fiber is fabricated with different material deposition. By using a double deposition of a metallic and a dielectric layer on a uniform-waist tapered optical fiber (Sym DLUWT) it is possible to eliminate the polarization of the plasmon excitation [43].

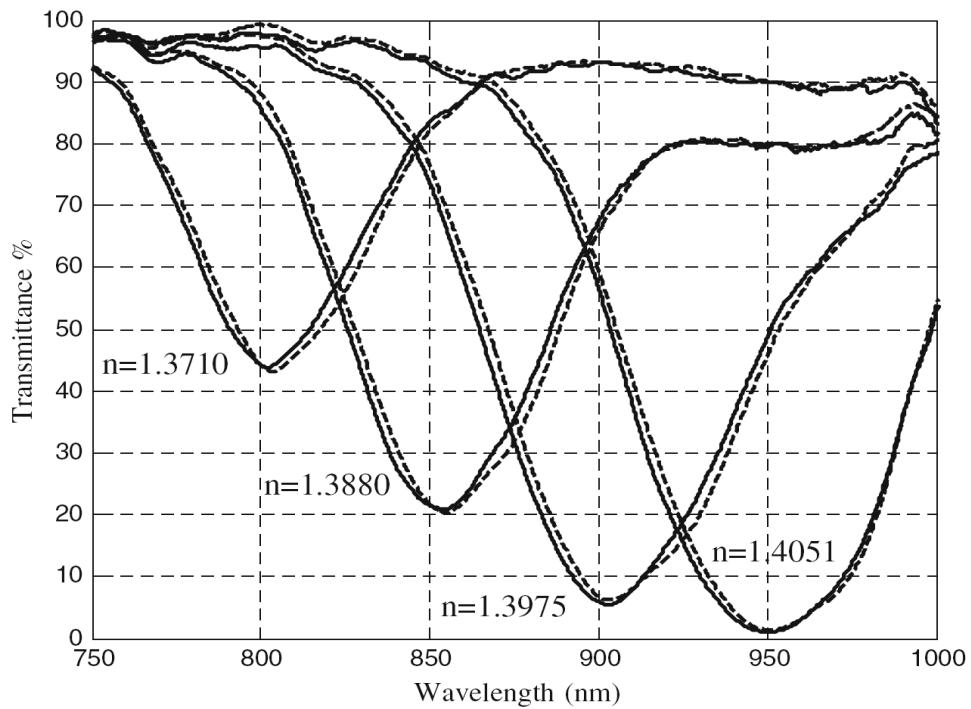


Figure 6.12: Polarization independence characteristics of the symmetrical DLUWT (Reprinted with permission-[68])

In the Fig. 6.12 the SPR shown as- dashed lines correspond to the use of polarization controlling elements and solid lines represent without use of the polarization controlling elements (Sym-DLUWT). It is clear that the performance is same for both cases by using the polarization controlling elements and by using Sym-DLUWT fiber. So if we use Sym-DLUWT it is possible to make polarization independent fiber which supports the SPR.

CHAPTER VII

Efficient Design Considerations

It is discussed earlier that the FBG can be produced in the core with some tilting angle so that the reflected wave becomes the cladding mode. But in that case the input wavelength was fixed. Here discussion is conducted to identify the way how to change or vary the input wavelength inside the fiber so that the sensor can be used with more flexibility. So the idea is to use Tilted Chirped Fiber Bragg Grating (TCFBG). Before discussing, it is necessary to consider the characteristics of CFBG.

Fig. 7.1 shows a chirped grating with length L_g and chirped BW $\Delta\lambda_{chirp}$. And this BW is related as [44]-

$$\Delta\lambda_{chirp} = 2n_{eff} (\Lambda_{long} - \Lambda_{short}) = 2n_{eff} \Delta\Lambda_{chirp} \quad (7.1)$$

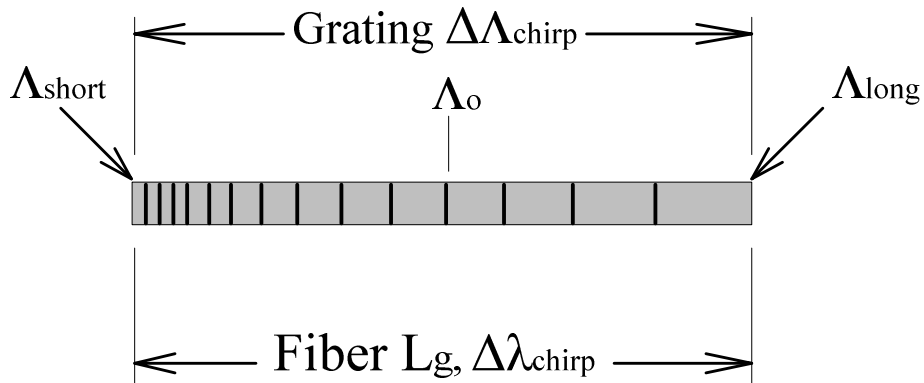


Figure 7.1: Chirped grating

The phase matching condition for the grating can be written as-

$$\lambda_{Bragg} = 2\Lambda_g n_{eff} \quad (7.2)$$

where Λ_g is the period of the grating section.

How many steps will be in a chirped grating that can be formulated as-

$$\frac{N}{L} = \frac{2n_{eff}\Delta\lambda_{chirp}}{\pi\lambda_{Bragg}^2} \quad (7.3)$$

where λ_{Bragg} is the central Bragg wavelength of the grating.

Now using $L_g = 100$ mm, $\Delta\lambda_{chirp} = 0.75$ nm & Bragg wavelength 1550 nm they [44] got 200 sections with 2 steps/mm and next 42 steps was used with 0.42 steps/mm. For both cases the reflectivity characteristic was approximately the same. So we can say that if we vary the sections of the grating from lower to higher or vice versa the reflectivity characteristics remain approximately the same. To get a clear concept they consider another case with 4 mm long grating and 2, 3 & 50 sections and got the same result.

So from the above discussion we can say that reflection characteristic of a CFBG is not completely dependent on the step size of the grating. Considering these characteristics-

- the idea is to introduce several TFBG with different period (Tilted Chirped FBG) in the fiber core so that each section of the TFBG can reflect different wavelengths as shown in the Fig. 7.2.
- to decrease the reflection inside the cladding, we may use some sort of anti reflection coating (ARC) inside the cladding to get maximum transmission of the wave reflected from the TFBG. So that maximum reflected cladding mode can reach at the metal-dielectric interface. We will be analyzing the properties about the ARC in the next section to check the possibility of using it in the sensor.
- we will be considering the gold layer (with 50-65 nm thickness) as a metal thin film, so that the surface plasmon can exist at metal-dielectric interface of the sensor.

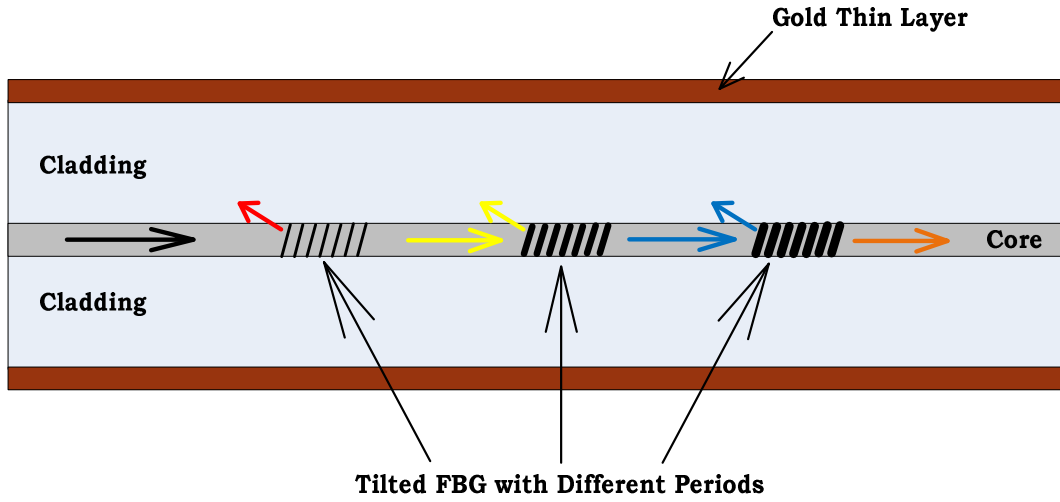


Figure 7.2: Proposed MW sensor using Tilted Chirped FBG concept

There are several things we need to consider:

The coupling condition for this case is [45]-

$$\lambda_{resonance}^i = \left(n_{eff}^{core} + n_{eff}^{cladding^i} \right) \Lambda \quad (7.4)$$

where $\lambda_{resonance}^i$ is the i th resonance of i th cladding mode, n_{eff}^{core} , $n_{eff}^{cladding^i}$ are the effective indices of core and cladding modes respectively and Λ is the period of the FBG. As we will be using the tilted FBG so the angle consideration need to be involved in (7.4). The tilting angle of the grating plane with respect to the axis of the fiber, need to be considered. So the modified grating period becomes-

$$\Lambda_g = \frac{\Lambda}{\cos \theta} \quad (7.5)$$

where θ is the tilting angle. Using (7.4) & (7.5) we get the final equation as-

$$\lambda_{resonance}^i = \left(n_{eff}^{core} + n_{eff}^{cladding^i} \right) \frac{\Lambda}{\cos \theta} \quad (7.6)$$

If we use three Tilted CFBG then we can have three reflected wavelength which can excite the surface plasmon. As a result we can have the wavelength flexibility. This can be compared with the result as reported in [45]. They inscribed two Bragg grating with different periods in a same fiber core.

For the first FBG the SP-resonance wavelength found was approximately at $0.77 \mu\text{m}$ but for the second FBG with different period the SP-resonance wavelength was approximately at $0.81 \mu\text{m}$. So by using chirped FBG the SP waves can be excited and resonance occurred with various wavelengths.

The sensor characteristic also depends on the refractive index change, FBG length variation and thickness of the gold layer. In [45] they used refractive index variation of 1×10^{-3} , 3×10^{-3} & 5×10^{-3} and found different transmissions for example at 46th mode the approximate transmission were 0.98, 0.70 and 0.38 respectively. Next they used Bragg grating length of 1 mm, 2 mm and 3 mm and found different transmission peaks, at 46th mode the approximate transmission were 0.84, 0.57 and 0.38 respectively. Finally they vary the thickness of the thin metal film, they used 40 nm, 50 nm and 60 nm and got abrupt change in the transmission peaks and wavelength shifts, at 46th mode the approximate transmission were 0.35, 0.39 and 0.30 respectively. The related wavelength shifts observed for 46th mode were $0.8086 \mu\text{m}$, $0.8087 \mu\text{m}$ and $0.80875 \mu\text{m}$ respectively.

For better performance we may make the cladding of the optical fiber of the sensor using anti reflection coating (ARC) materials. To check the possibility of using ARC materials as cladding we first consider the characteristic of the ARC. To do so we considered two material systems in such a way that the plasmon wave exist at the metal-ARC interface -

- i) Effect of ARC for SOI material system
- ii) Effect of ARC for SOS material system

7.1 Effect of ARC for SOI Material System

The propagation of electromagnetic waves generated from any light source normally influenced by the layered stack of media. The travelling light waves will be reflected, transmitted, refracted multiple times by interfaces between different media. So, different waves will present to the electromagnetic field in each layer of the stack which results interference phenomena [46], [47]. Some of the light incident on the stack of layers will be transmitted, part of it will be absorbed and part of it will be reflected. Maximum transmission and minimum reflection is desired at many applications. One of these applications is the antireflection (AR) coating, the design and fabrication method is discussed in [48].

One example of this AR coating is the efficient coupling of light from a fiber to waveguide or photonic integrated circuit and its surrounding medium. This AR coating is used in several related applications [49]-[51] A general case is considered here- an antireflection coating is developed so that the transmission of the guided mode of the waveguide structure through the interface between the photonic integrated circuit and its surrounding medium (air) is maximized [52] and to observe the polarization effect of light on antireflection coating. This AR coating is also used in telecommunication application [53].

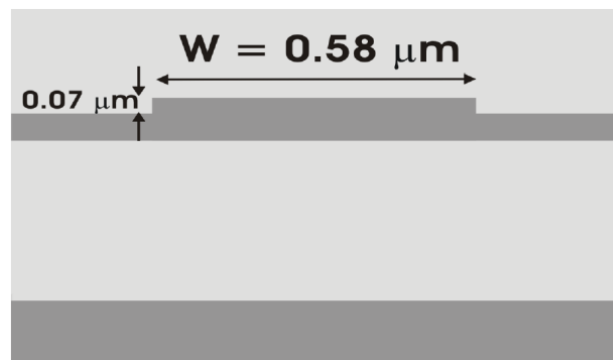


Figure 7.3: Waveguide facets for SOI material system

At the end facets (input and output side) of a photonic integrated circuit light is coupled respectively from and to an optical fiber. In order to maximize the transmission for horizontal coupling an antireflection coating can be deposited on the facets of the chip. Such an antireflection coating consists of a stack of thin films with accurately chosen thicknesses and refractive indices. For our analysis we will be considering the system as shown in Fig.7.7. The guided mode of the waveguide is assumed as a Gaussian beam. In Table 7.1 the properties of this beam are given, σ_x and σ_y are the typical dimensions of the Gaussian function.

In Essential Macleod all layers of a stack are homogeneous. In this case the substrate is the cross section of a waveguide structure, which obviously is not homogeneous. Consequently, we modeled this cross-section by one single number, i.e. the effective index n_{eff} of the guided mode of the waveguide. Here λ_0 is the wavelength.

Table 7.1: Dimensions of the Gaussian field profile for SOI

Material System	λ_0 [μm]	σ_x [μm]	σ_y [μm]	n (n_{eff})
SOI	1.55	0.39	0.46	2.7

7.1.2 Design & Simulation of AR Coating

First a single-layer coating is designed, then it is optimized and finally design of a multi-layer coating is conducted with the aid of the CAD tool Essential Macleod.

We consider the transmission at the interface of the waveguides (Fig. 7.3). In Essential Macleod we can only calculate the transmission through a stack of homogeneous layers, so we model the cross section of the waveguide structure by one single number, the effective index n_{eff} of the guided mode of the structure.

The CAD software enables us to calculate the transmission of plane waves incident at an arbitrary angle, but the guided modes of the waveguide structures are approximated by Gaussian beams (the properties of which are given in Table 7.1). We can solve this problem by decomposing the Gaussian beam into its plane wave components through spatial Fourier transform, calculating the transmission for each of these components and then using the inverse Fourier transform to obtain the transmitted beam.

The transmission through a layer stack is calculated, which is built up of a semi-infinite substrate layer (in this case the waveguide), a number of thin films and another semi-infinite medium (in this case air). The thickness of each layer can be set by a physical thickness and by an optical thickness. The optical thickness is equal to the number of wavelengths the layer contains:

$$\text{Optical thickness} = \frac{\text{physical thickness}}{\lambda/n}$$

7.1.3 Result & Analysis

7.1.3.1 Without AR coating

To have clear understanding first of all, the measurement was conducted without any coating so that we can use it as reference. In this case there is no transmission above critical angle i.e.

$$\text{Critical angle} = \sin^{-1}\left(\frac{1}{2.7}\right) = 21.74^\circ$$

We also observed 100% transmission at Brewster angle i.e.

$$\text{Brewster angle} = \tan^{-1}\left(\frac{1}{2.7}\right) = 20.32^\circ$$

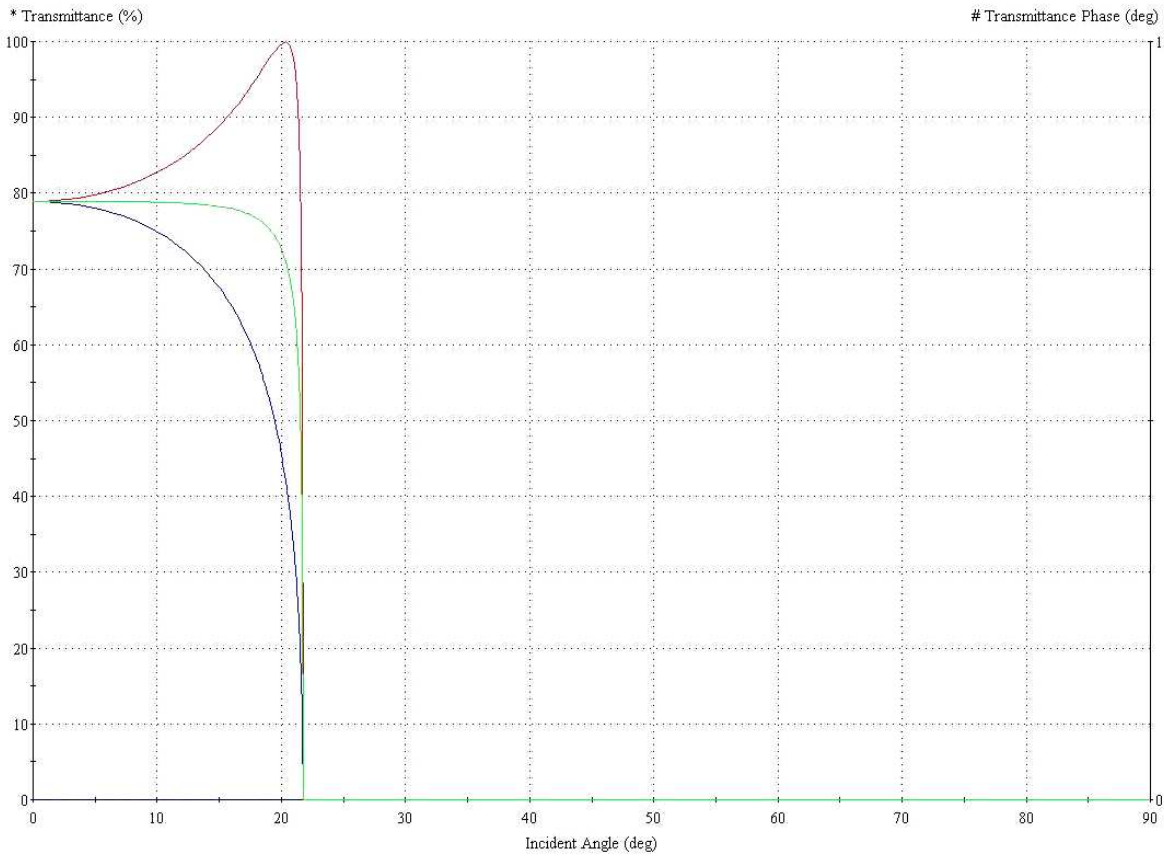


Figure 7.4: Transmission for all polarizations when there is no coating: magnitude (solid lines) and phase (dashed lines). TM: red, TE: blue, Mean: green

For perpendicular incidence (incident angle= 0°) transmission can be calculated [54] as-

$$r = \frac{n_{eff} - 1}{n_{eff} + 1} = 0.46$$

$$T = 1 - R = 1 - r^2 = 79\%$$

The phase is zero everywhere i.e. Phase = 0.

Because there is no coating, as a result no phase change and no interference.

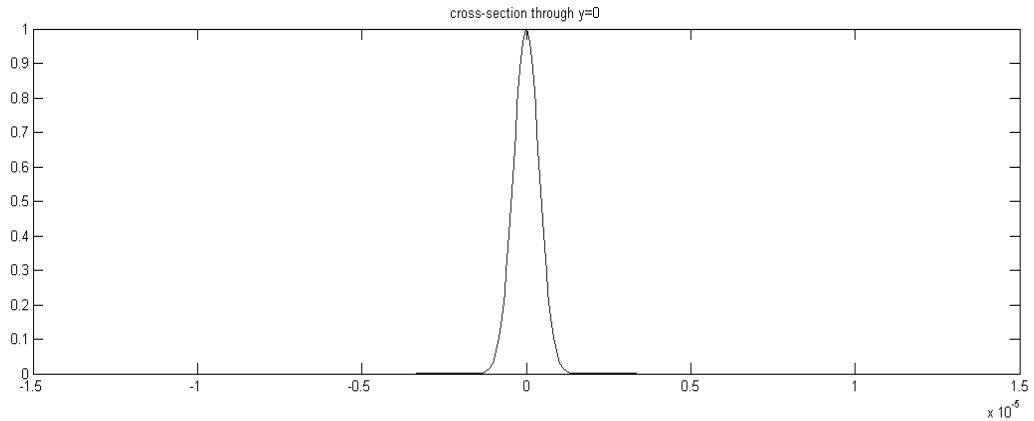


Figure 7.5: Input field amplitude

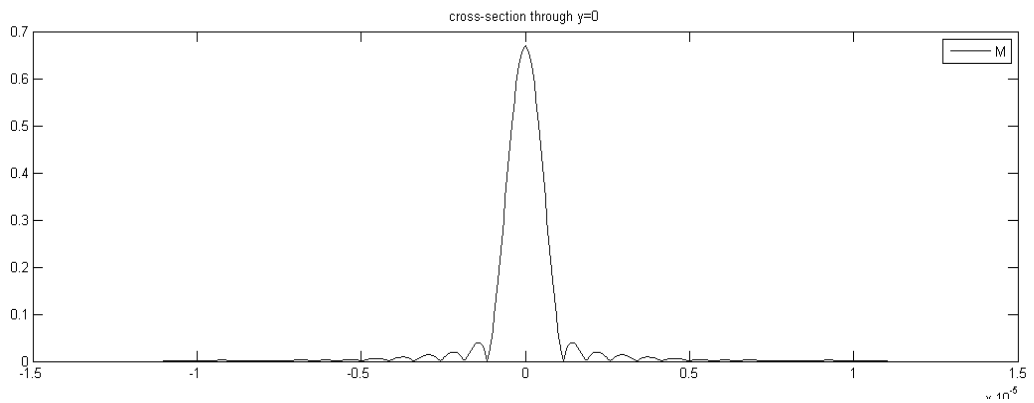


Figure 7.6: Output field amplitude (mean)

From the Fig. 7.4 it is clear that Transverse-Electric (TE) polarized light transmission is slightly lower than the Transverse-Magnetic (TM) polarized light because of the Brewster angle but both polarizations (TE & TM) have similar amplitude profile. As there is no coating it is desired that there will be no interference at the output. The output should be same as the input (Fig. 7.5). But it is clear from the Fig.7.6 that there are interferences at the output. These interference fringes around the edges of the Gaussian beam because the beam width is small compared to the wavelength, which causes diffraction. Global transmission is calculated using the Table 7.1 parameters and MATLAB simulator. Thus we get global transmission as-

TM Polarized Light = 79.6163%

TE Polarized Light = 67.3830%

Mean = 73.4983%

As expected, the global value is slightly lower than the value for perpendicular incidence because the Gaussian beam also has plane wave components with a more oblique incidence, for which the transmittance is lower (Fig.7.4).

7.1.3.2 One layer AR coating

Theoretical values for single layer coating can be calculated as [55],[56]-

$$n_{AR} = \sqrt{2.7} = 1.64$$

$$physical\ thickness = \frac{1}{4} \cdot \frac{\lambda}{n_{AR}}$$

So, layer thickness is 236.25 nm.

According to the Snell's law-

$$n_{SOI} \cdot \sin(\theta_{SOI}) = n_{AR} \cdot \sin(\theta_{AR}) = n_{air} \cdot \sin(\theta_{air})$$

Critical angle when $\theta_{air} = 90^\circ$ or $\theta_{AR} = 90^\circ$ is-

$$\theta_{SOI,crit} = \min \left\{ \sin^{-1} \left(\frac{n_{air}}{n_{SOI}} \right), \sin^{-1} \left(\frac{n_{AR}}{n_{SOI}} \right) \right\}$$

$$= \sin^{-1} \left(\frac{n_{air}}{n_{SOI}} \right) = 21.74^\circ$$

In this case the phase change will be different for TE & TM polarization.

Due to the fact that there is a phase change, the different plane wave components of the Gaussian beam will interfere with each other. This will cause a lower transmission as we see in Fig. 7.8.

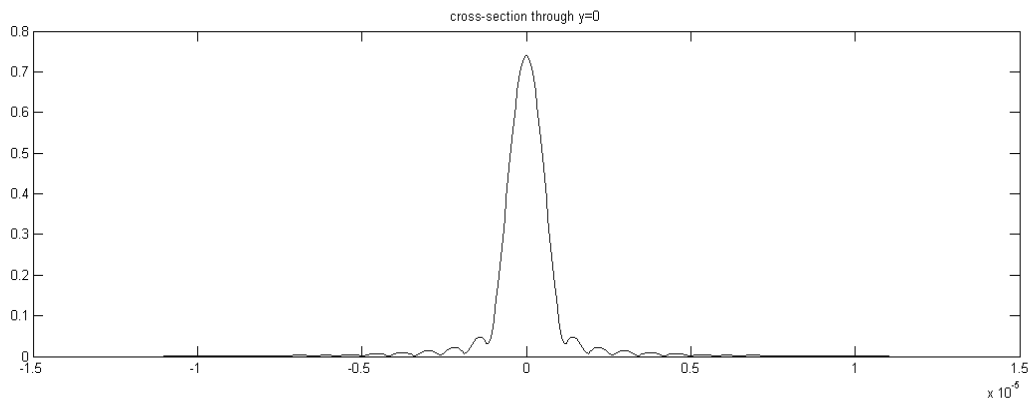


Figure 7.7: Output field amplitude (Mean)

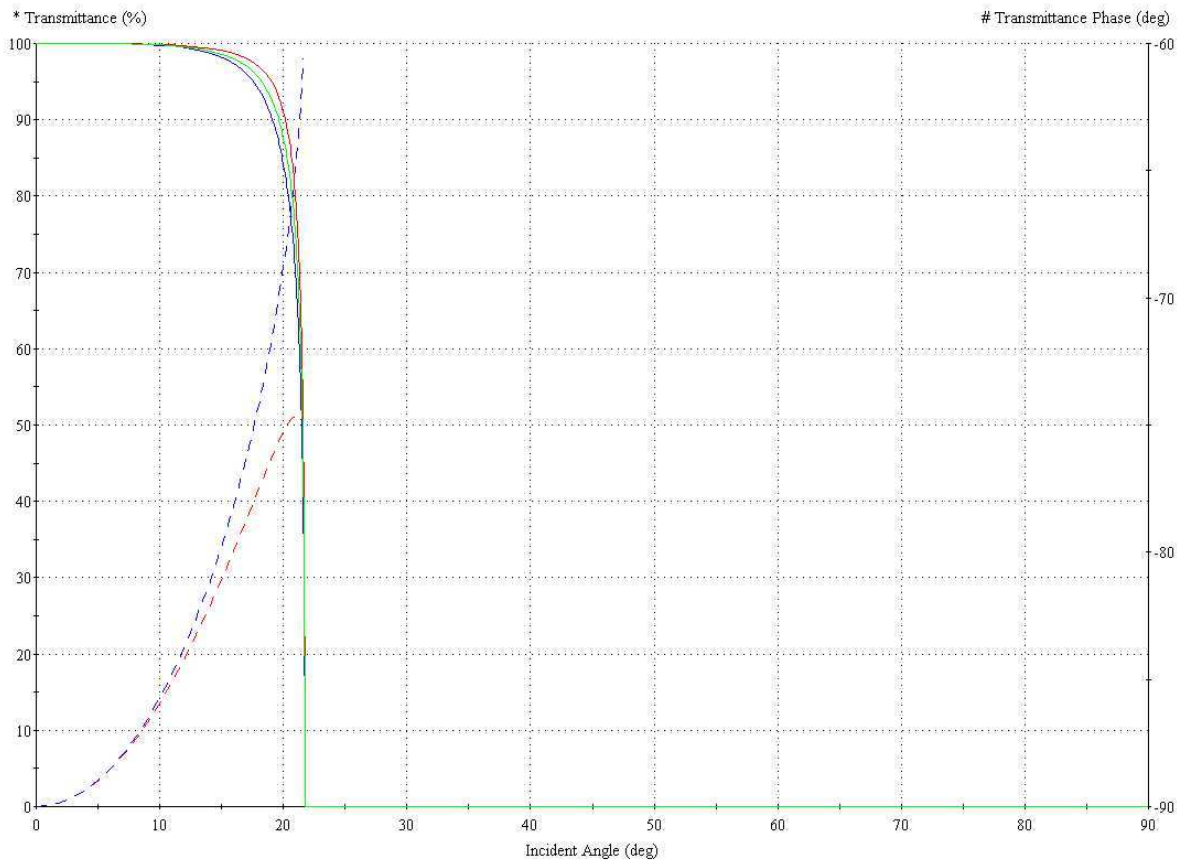


Figure 7.8: Transmission for all polarisations for a single layer coating: magnitude (solid lines) and phase (dashed lines). TM: red, TE: blue, Mean: green

Mean transmission shows stronger interference fringes, TM also shows slightly stronger interference than TE.

TM-transmission is slightly higher than TE-transmission: smaller phase shift for TM than for TE (Fig.7.8) results less interference of the plane waves.

Global transmission is-

TM Polarized Light = 93.0245 %

TE Polarized Light = 92.2584%

Mean = 92.6414%

The transmission is much lower than expected, because of the interference effects.

7.1.3.3 Optimized one layer AR coating

Optimization of the coating was done by changing the thickness of the layer to increase the transmission. We set the targets to a wavelength of 1550 nm, and 100% transmission between 0° and different angles. We obtained the best results for an angle range of 0°-15°. The optimized physical thickness is 246.97 nm.

Global transmission is-

TM Polarized Light = 93.0440 %

TE Polarized Light = 92.6245%

Mean = 92.8342%

The transmission is slightly higher comparing with the case of no optimization.

7.1.3.4 Multi layer AR coating

Optimization for higher transmission with multiple layers is considered here. The layers were maximum 5; this will limit calculation time and is also more realistic: adding more layers will complicate the fabrication.

When we use the above targets, the simulator generates a one-layer coating identical to the one we used in the previous section. Using different targets did not help us to find a better solution, on the contrary: some of the multi-layer coatings we created gave a lower transmission than the one layer coating.

So, if we use the antireflection coating to maximize the transmission; we get on an average 19% more transmission than if we use no antireflection coating. The main concern goes to polarization, when there is no AR coating the difference between TM polarized light transmission (79.6163%) and the TE polarized light transmission (67.3830%) is high.

But when we use AR coating the light transmission difference between the TM (93.0245 %) & TE (92.2584%) polarized light become smaller. So by using AR coating we can reduce the polarization effect of lights. Though AR coating reduces the polarization effect but TM polarized light transmission is always higher than the TE polarized light. This type of investigation can also be conducted for Silica on Silicon (SOS) and other material system to find out the optimized way to use AR coatings regarding polarization and maximum transmission of light.

7.2 Effect of ARC for SOS Material System

Reflection is the optical phenomenon, which is born out of a transition in the medium in which light is travelling. Any optical medium is characterized by the parameter which is known as refractive index (n) and quantifies the speed of light in the current medium with respect to that in vacuum. Normally a fraction of incident light reflected from the interface of an optical medium is measured by reflectance, and the rest transmitted (refracted) is measured by transmittance. The mathematical model to calculate the refractive index of the thin film is the same as mentioned earlier [55], [56]-

$$n_{AR} = \sqrt{n_1 n_2}$$

$$physical\ thickness = \frac{1}{4} \cdot \frac{\lambda}{n_{AR}}$$

where, n_{AR} is the refractive index of the thin film, n_1 & n_2 are the refractive index of the related two medium and λ is the wavelength of the light.

The first material system applied for fabricating commercial photonic integrated circuits for telecom applications on silicon was silica. Thanks to the very low loss of straight waveguides (0.03dB/cm) at a wavelength of $\lambda= 1550$ nm. The downside of this material system however is the low refractive index contrast of this material which implies huge bends and therefore huge components.

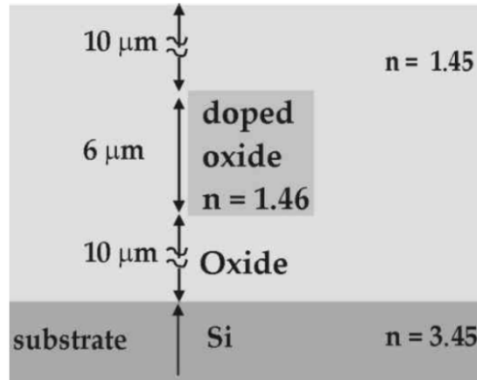


Figure 7.9: Cross-section of a waveguide fabricated in silica on silicon.

To fabricate a waveguide in silica on silicon (Fig.7.9), is done by heavily doping of a SiO_2 layer with germanium is required. This results a refractive index difference of about 0.75% with the undoped SiO_2 . A waveguide is defined in the doped SiO_2 through an etching process, and afterwards an undoped SiO_2 cladding layer is deposited. Anti reflection coatings (ARC) are designed for different purposes [57], but here we considered the analysis in general to get a general characteristic of the ARC in case of SOS material system.

Here we analyzed the transmission of the guided mode of the waveguide structure through the interface between the photonic integrated circuit and its surrounding medium (air). We want to maximize the transmission, to achieve this we use a single-layer coating, which we then optimize and finally we design a multi-layer coating with the aid of the CAD tool Essential Macleod. We analyzed the transmission for Silica on Silicon (SOS) material system in the similar manner as we did for SOI material system. The transmittance can be increased using the ARC [62].

7.2.1. Simulation

By using the CAD software we can calculate the transmission of plane wave incident at an arbitrary angle. But the guided modes of the waveguide structures are approximated by Gaussian beam. The properties of this Gaussian beam are given in Table 7.2. We solved this problem by decomposing the Gaussian beam into its plane wave components using the spatial Fourier transform, calculating the transmission for each of these components. Afterwards using the inverse Fourier transform we obtain the transmitted beam.

Table 7.2 Dimensions of the Gaussian field profile for SOS.

Material System	λ_0 [μm]	σ_x [μm]	σ_y [μm]	n (n_{eff})
Silica on Silicon (SOS)	1.55	3.63	3.63	1.455

In Essential Macleod we calculate the transmission through a layer stack, which is built up of a semi-infinite substrate layer (in this case the waveguide), a number of thin films and another semi-infinite medium (in this case air). The thickness of each layer can be set by a physical thickness and by an optical thickness. The optical thickness is equal to the number of wavelengths the layer contains:

$$\text{Optical thickness} = (\text{Physical thickness})/(\lambda/n)$$

7.2.3. Findings & Analysis

7.2.3.1. Without Coating

We consider the transmission of light for the SOS material system without any AR coating. This transmission was conducted to consider it as the reference. The input field amplitude is shown in Fig. 7.11. This input field was used throughout the whole simulation, so that we can compare among all the results easily and effectively.

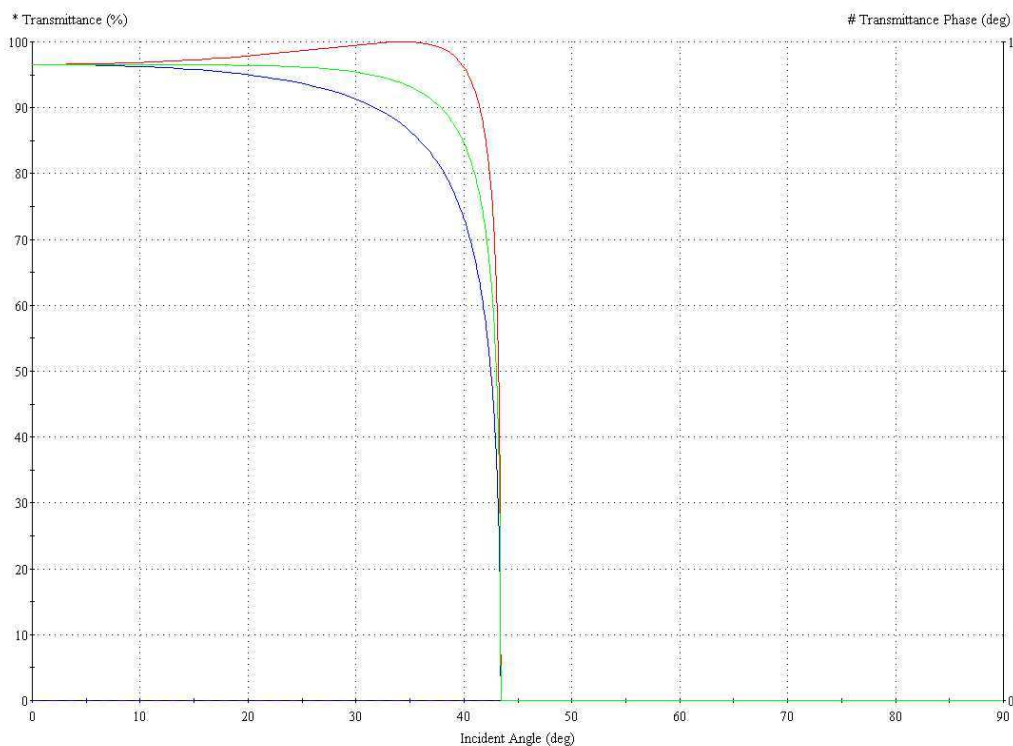


Figure 7.10: Transmission for all polarisations when there is no coating: magnitude (solid lines) and phase (dashed lines). TM: Red, TE: Blue, Mean: Green.

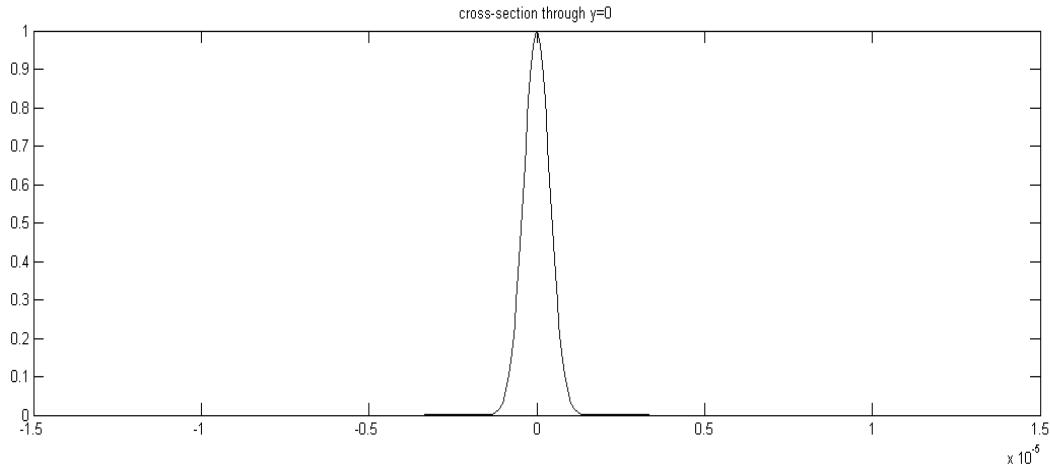


Figure 7.11: Input field amplitude.

In case of without coating critical angle is 43.42° . Angle consideration of ARC for the telecom wavelength can be found in [63]. It is clear from the Fig. 7.10 that there is no transmission above the critical angle. We also noticed, there is 100% transmission for TM-polarisation at Brewster angle [64]. i.e.-

$$\text{Brewster angle} = \tan^{-1}\left(\frac{1}{1.455}\right) = 34.50^\circ$$

It is observed that the calculated and the simulated Brewster angle is the same. Next we considered the transmission for incident angle = 0° (perpendicular incidence):

$$r = \frac{n_{eff} - 1}{n_{eff} + 1} = 0.19$$

$$T = 1 - R = 1 - r^2 = 97\%$$

So the transmission for perpendicular incidence is 97% and this also matched with the simulated result as shown in Fig.7.10. Phase is zero everywhere in the figure. There is no coating so no phase shift for transmission through an interface as a result no interference occurred. Because of the Brewster angle the TE-transmission is slightly lower than TM-transmission but has similar amplitude profile. No interference fringes around the edges of the Gaussian beam were observed because the beam width is large compared to the wavelength.

Global transmission was calculated using the Table 7.2 parameters and MATLAB simulator.

Global transmission:

TM Polarized Light = 96.5871 %

TE Polarized Light = 96.5428%

Mean = 96.5650%

As expected, the mean value is slightly lower than the value for perpendicular incidence because the Gaussian beam also has plane wave components with a more oblique incidence (referring to Fig.7.10).

7.2.3.2. Single Layer Coating

Theoretical values for coating:

$$n_{AR} = \sqrt{1.455} = 1.206$$

$$physical\ thickness = \frac{1}{4} \cdot \frac{\lambda}{n_{AR}}$$

We considered a material with n close to this value- Na₃AlF₆: n' = 1.35; n'' = 0

Results from the simulation are as follows-

- Critical angle when $\theta_{air} = 90^\circ$ or $\theta_{AR} = 90^\circ$:

$$\theta_{SOS,crit} = \min \left\{ \arcsin \left(\frac{n_{air}}{n_{SOS}} \right), \arcsin \left(\frac{n_{AR}}{n_{SOS}} \right) \right\} = \arcsin \left(\frac{n_{air}}{n_{SOS}} \right) = 43.42^\circ$$

- Phase change is different for TE & TM polarization.

The phase change is observed due to the interference of the different plane wave components of the Gaussian beam. This will cause a lower transmission.

- TM-transmission is slightly higher than TE-transmission because of smaller phase shift for TM than for TE (referring to Fig.7.13). i.e. less interference of the plane waves.
- Global transmission:

TM Polarized Light = 98.7524 %

TE Polarized Light = 98.7329%

Mean = 98.7427%

These transmission values are better than the ones for silicon on insulator (SOI) material system [59]. This is because the beam width of the Gaussian beam is relatively larger compared to the wavelength, so the plane wave decomposition will be less spread out. The critical angle is also much larger than for SOI, so less plane wave components will be completely lost. Single layer reflectance can be calculated using [60]. The result is shown in Fig.7.13 and can be compared with the reflectance in [61], [65] which are similar.

7.2.3.3. Optimized Single Layer Coating

We optimized the transmission of the coating by changing the thickness of the layer using *Simplex*. The optimization leads to a thickness very close to the theoretical value, and there is no difference in the transmission values of the Gaussian beam.

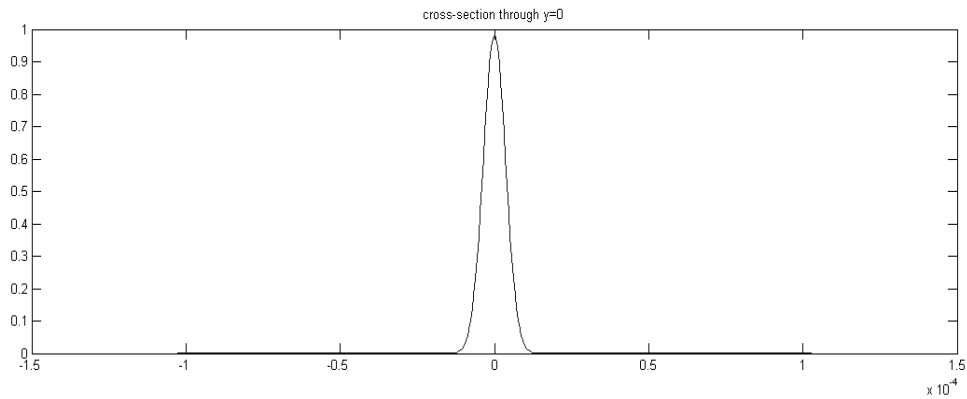


Figure 7.12: Output field amplitude (mean)

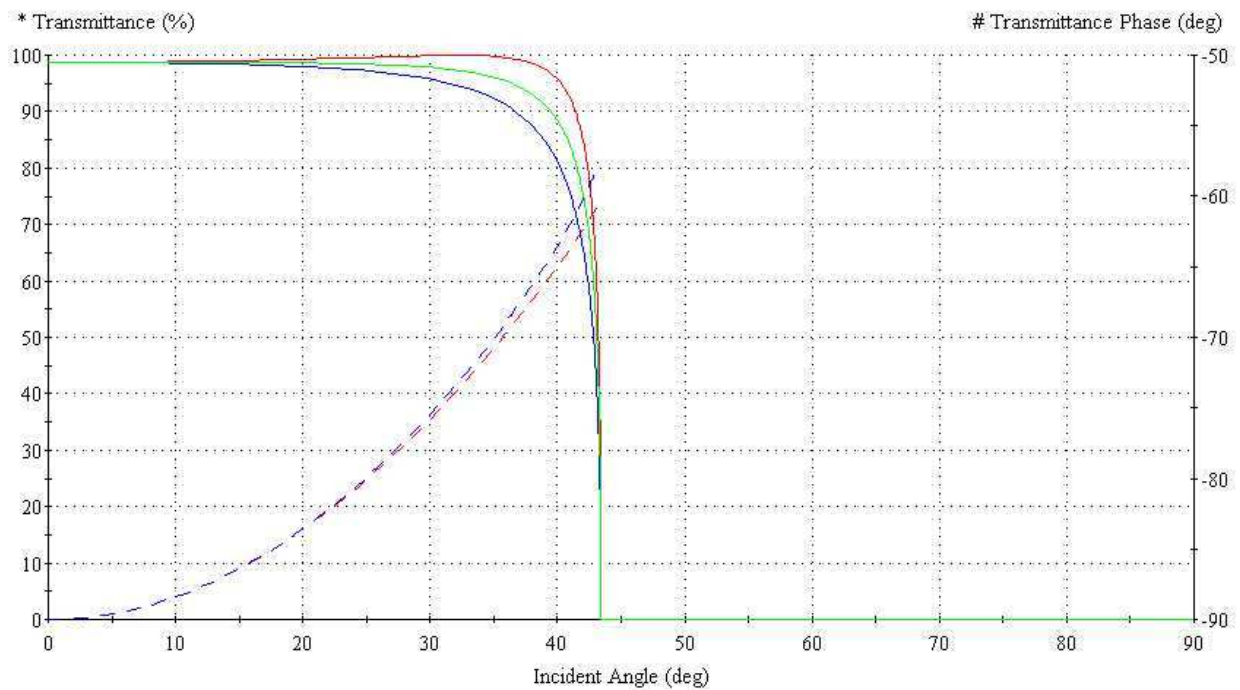


Figure 7.13: Transmission for all polarisations for a 1 layer coating: magnitude (solid lines) and phase (dashed lines). TM: Red, TE: Blue, Mean: Green.

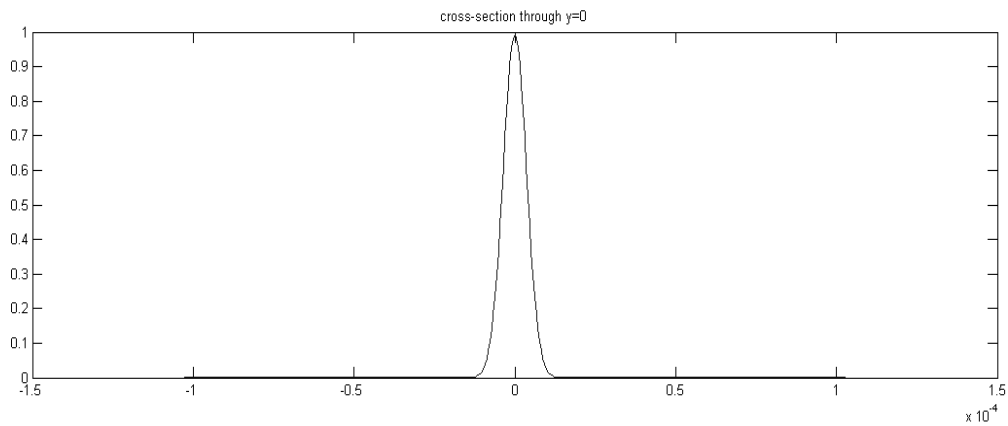


Figure 7.14: Output field amplitude (mean).

Table 7.3: Multilayer coating design for SOS

Layer	Material	Refractive Index	Extinction Coefficient	Optical Thickness	Physical Thickness (nm)
Medium	SOS	1.45500	0.00000	-	-
1	Na ₃ AlF ₆	1.35000	0.00000	0.23865533	274.01
2	MgF ₂	1.37600	0.00000	0.04876160	54.93
3	Al ₂ O ₃	1.64974	0.00000	0.08543824	80.27
4	MgF ₂	1.37600	0.00000	0.11674291	131.51
5	Na ₃ AlF ₆	1.35000	0.00000	0.23325150	267.81
Substrate	Air	1.00000	0.00000	-	-
-	-	-	0.00000	0.72284958	808.52

Incident Angle: 0°; Reference Wavelength: 1550 nm

7.2.3.4. Multilayer Coating

Next we optimize the transmission with multiple layers (maximum 5) using *Optimac*. We did not use metals in the coating because metal absorbs the field, nor do we use water because it is impossible to fabricate a liquid coating.

We set the targets to a wavelength of 1550 nm, and 100% transmission for 0°-10°. Design details are given in Table 7.3.

There is almost no reflection of the Gaussian beam when we use this coating. The wave characteristics in multilayered structure can be analyzed using [54].

Global transmission:

TM Polarized Light = 99.9952 %

TE Polarized Light = 99.9947%

Mean = 99.9949%

Results in general are better for SOS because the refractive index contrast is lower than for SOI. We expected a better performance of the multilayer coating compared to the single layer coating. For SOS this is true, for SOI however, the optimized single layer coating gave the best result. The mean transmission 2.1777% and 3.4299% are increased by using single layer and multilayer coating respectively using SOS material system comparing with the reference (without coating).

From the above discussion and simulation result we can say that it will be helpful for the sensor if we can make the cladding layer by using some ARC materials as shown in Fig. 7.15. The ARC materials need to be a dielectric (as example MgF_2) and must have the refractive index less than the core medium of the fiber. If it is possible to use the ARC materials as cladding the transmission of the cladding mode through the cladding will be maximum because of less reflections. As a result maximum cladding mode will appear at the metal-dielectric interface and it will excite maximum surface plasmon waves. So the SPR will be higher and the efficiency of the sensor will be increased. As the TM polarized wave has the maximum transmission through ARC materials so it will also helpful for this sensor application because at SP wave only TM mode exists. But further study requires regarding the use of ARC materials as a cladding. For the tilting angle we can consider the result of [66]. The tilting angle need to be used within $0-10^\circ$. If the tilting angle exceeds 15° then there will be a huge polarization effect.

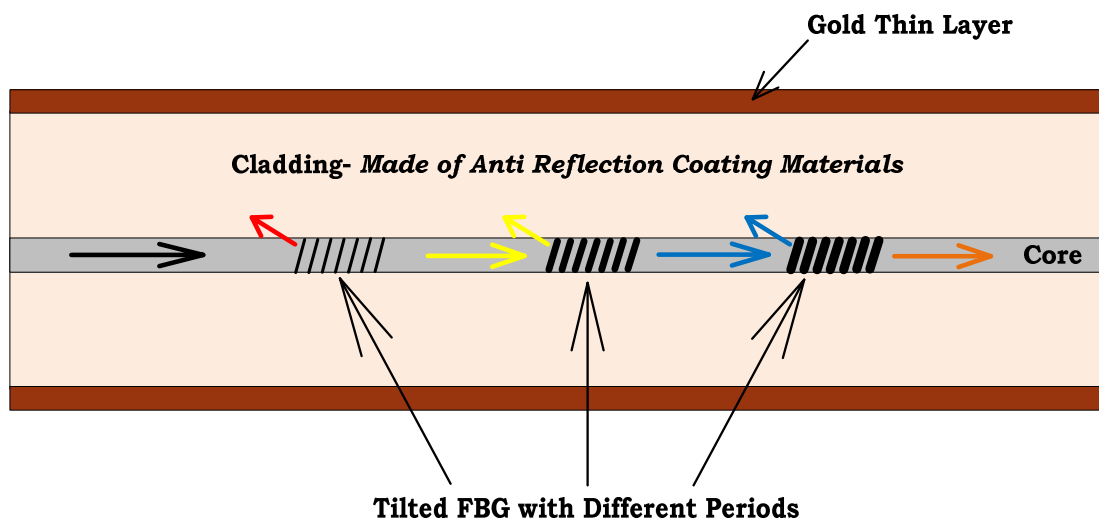


Figure 7.15: Proposed MW sensor using TCFBG concept and ARC materials as cladding.

CHAPTER VIII

Conclusion & Future Works

A new type of MW sensor is proposed. Microwave (MW) detection based on surface plasmon resonance fiber optic sensors is analyzed. SPR can be obtained by using the TFBG or other configurations (like hetero core fiber). The SPR wave is dependent on various factors like the thickness of the metal layer, polarization dependence etc. MW can penetrate few nm in the metal so the metal film layer needs to be carefully designed. The detection of the MW is only possible by the SPR based fiber optic sensor when the SPR will be affected by the impinging MW on the metal surface through heating in the metal. The range of MW that can be detected in this way depends on the metal film layer thickness and the type of metal used for the generation of SPR. In this work the MW detection scheme is described using SPR based sensor, considering the SPR generation, polarization, Bragg wavelength shift, metal film thickness, corresponding temperature effects or thermo-optic effect and the use of ARC materials as a cladding. But the power or energy of the MW frequency, amplitude of the MW frequencies, the different band of MW frequencies and the realization of ARC materials as cladding & realization of bended waveguide configuration with thin gold layer for SPR generation are not considered here. ARC materials for cladding need to be transparent also. There could be an effect of high power/energy MW frequency and low power/energy MW frequency on sensing. More analysis needs to be done on this area. The main limitation of this scheme to sense MW will be the cost of the elements those are necessary to build the sensor. On the other hand the main advantage of this proposed sensor is that it will be very small in size so that it can be integrated with other micro-electronic devices very easily.

REFERENCES

1. E. Udd, *Fiber Optic Sensors: An Introduction for Engineers and Scientists*, John Wiley and Sons, New York, 1991.
2. M.D.Marazuela, M.C.Moreno-Bondi, "Fiber optic biosensor-an overview", *Anal Bioanal Chem* (2002) 372: 664-682.
3. Anuj K. Sharma, Rajan Jha, H.S.Pattanaik, G.J. Mohr, "Design considerations for surface plasmon resonance-based fiber-optic detection of human blood group", *Journal of Biomedical Optics*, 14(6), 064041 (Nov/Dec 2009).
4. R. Slavik, J. Homola, J. Ctyroky, E. Brynda, "Novel spectral fiber optic sensor based on surface plasmon resonance", *Sens. Actuators, B* 74 (2001) pp.106-111.
5. M. Piliarik, J. Homola, Z. Manikova, J. Ctyroky, "Surface plasmon resonance sensor based on a single mode polarization maintaining optical fiber", *Sens. Actuators, B* 90 (2003) pp.236-242.
6. D. Monzon-Hernandez, J. Villatoro, D. Talavera, D. Luna-Moreno, "Optical fiber surface-plasmon resonance sensor with multiple resonance peaks", *Appl. Optics*, 43 (2004) pp. 1216-1220.
7. Anuj K. Sharma, Rajan Jha, and B. D. Gupta, "Fiber-optic sensors based on surface plasmon resonance: A Comprehensive Review," *IEEE Sensors Journal*, vol. 7, no. 8, August 2007.
8. Jiří Homola, "Present and future of surface plasmon resonance biosensors," *Anal Bioanal Chem* (2003) 377: 528–539.
9. Katherine A.Willets and Richard P. Van Duyne, "Localized surface plasmon resonance spectroscopy and sensing," *Annu. Rev. Phys. Chem.* 2007. 58:267–97.
10. K.O.Hill and G. Meltz, "Fiber Bragg Grating Technology Fundamentals and Overview", *Journal of Lightwave Technology*, Vol. 15, No. 8, August 1997.
11. G.P. Agrawal, *Fiber-Optic Communication Systems*, (John Wiley & Sons, 2002).
12. F. Baldini, A. N. Chester, J. Homola, and S. Martellucci, Eds. (2004) "Optical Chemical Sensors", *NATO Science Series* Vol. 224.
13. G. Meltz, S. J. Hewlett, and J. D. Love (1996) "Fiber Grating Evanescent-Wave Sensors", *Proceedings of SPIE Vol. 2836 Chemical, Biochemical, and Environmental Fiber Sensors VIII*, pp. 342–350.
14. K. Usbeck, W. Ecke, A. Andreev, V. Hagemann, R. Mueller, and R. Willsch (1998) "Distributed Optochemical Sensor Network Using Evanescent Field Interaction in Fiber Bragg Gratings", *Proceedings of 1st European Workshop on Optical Fibre Sensors*, 08–10 July 1998, Peebles, Scotland, SPIE Vol. 3483, pp. 90–94.
15. K. Schröder, W. Ecke, R. Mueller, R. Willsch, and A. Andreev (2001) "A Fibre Bragg Grating Refractometer", *Meas. Sci. Technol.*, Vol. 12, pp. 757–764.
16. A. Cusano, A. Iadicco, P. Pilla, L. Contessa, S. Campopiano, and A. Cutolo (2005) "Cladding Mode Reorganization in High-Refractive Index-Coated Long-Period Gratings: Effects on the Refractive-index Sensitivity", *Opt. Lett.*, Vol. 30, No. 19, October 1, pp. 2536–2538.
17. S. W. James, N. Rees, R. P. Tatam, and G. J. Ashwel (2002) "Optical Fiber Long Period Gratings With Langmuir-Blodgett Thin Film Overlays", *Opt. Lett.*, 9, pp. 686–688.
18. I. Del Villar, I. Matías, F. Arregui, and P. Lalanne (2005). "Optimization of Sensitivity in Long Period Fiber Gratings with Overlay Deposition", *Opt. Express*, Vol. 13, pp. 56–69.

19. A. Cusano, A. Iadicicco, P. Pilla, L. Contessa, S. Campopiano, A. Cutolo, and M. Giordano (2006) "Mode Transition in High Refractive Index Coated Long Period Gratings", *Opt. Express*, Vol. 14, pp. 19–34.
20. A. Asseh, S. Sandgren, H. Ahlfeldt, B. Sahlgren, R. Stubbe, and G. Edwall, (1998) "Fiber Optical Bragg Grating Refractometer", *Fiber and Integrated Optics*, Vol. 17, pp. 51–62.
21. A. Iadicicco, A. Cusano, S. Campopiano, A. Cutolo, and M. Giordano (2005) "Microstructured Fiber Bragg Gratings: Analysis and Fabrication", *IEE Electronics Lett.*, Vol. 41, No. 8, pp. 466–468.
22. B. Sutapun, M. Tabib-Azar, and A. Kazemi (1999) "Pd-Coated Elastooptic Fiber Optic Bragg Grating Sensors for Multiplexed Hydrogen Sensing", *Sens. Actuators B*, Vol. 60, pp. 27–34.
23. Y. Tang, T. Peng, J. S. Sirkis, B. A. Childers, J. P. Moore, and L. D. Melvin (1999) "Characterization of a Fiber Bragg Grating (FBG)-Based Palladium Tube Hydrogen sensor", in Proc. *SPIE Smart Structures Mater. Conf.*, 1999, vol. 3670, pp. 532–540.
24. Y. T. Peng, Y. Tang, and J. S. Sirkis (1999) "Hydrogen Sensors Based on Palladium Electroplated Fiber Bragg Gratings," in Proc. SPIE 13th Int. Conf. Opt. Fiber Sensors Workshop Device Syst. Technol. *Toward Future Opt. Fiber Commun. Sensing*, Vol. 3746, pp. 171–179.
25. R. R. J. Maier, J. S. Barton, J. D. C. Jones, S. McCulloch, B. J. S. Jones, and G. Burnell, (2006) "Palladium-Based Hydrogen Sensing for Monitoring of Ageing Materials," *Meas. Sci. Technol.*, Vol. 17, pp. 1118–1123.
26. T. Erdogan and J. E. Sipe (1996) "Tilted Fiber Phase Gratings", *J. Opt. Soc. Amer. A*, Vol. 13, pp. 296–313.
27. G. Laffont and P. Ferdinand, (2001) "Tilted Short-Period Fibre-Bragg-Grating induced Coupling to Cladding Modes for Accurate Refractometry" *Meas. Sci. Technol.* Vol. 12, pp.765–770.
28. G. Laffont and P. Ferdinand (2001) "Sensitivity of Slanted Fibre Bragg Gratings to External Refractive Index Higher than that of Silica" *Electronics Letters*, 1st March 2001 Vol. 37, pp. 321–328.
29. X. Chen, K. Zhou, L. Zhang, and I. Bennion (2005) "Optical Chemsensor Based on Etched Tiled Bragg Grating Structures in Multimode Fiber", *IEEE Phot. Technol. Lett.*, 17(4), 864–866.
30. C. Caucheteur and P. M'egret, (2005) "Demodulation Technique for Weakly Tilted Fiber Bregg Grating Refractometer," *IEEE Phot. Technol. Lett.*, Vol. 17, No. 12, pp. 2703–2705.
31. D. Paladino, P. Pilla, A. Cutolo, S. Campopiano, M. Giordano, A. Cusano, C. Caucheteur, P. M'egret (2007) "Effects of Thickness and External Refractive Index in Coated Tilted Fiber Bragg Gratings" *Proceedings of SPIE* Vol. 6619, pp. 68.
32. D. Paladino, A. Cusano, P. Pilla, S. Campopiano, C. Caucheteur, and P. M'egret (2007) "Spectral Behaviour in Nano-Coated Tilted Fiber Bragg Gratings: Effect of Thickness and External Refractive Index" *IEEE Phot. Technol. Lett.*, Vol. 19, No. 24, pp. 2051–2053.
33. Yanina Y. Shevchenko and Jacques Albert, "Plasmon resonances in gold-coated tilted fiber Bragg gratings," *Optics Letters*, vol. 32, no. 3, February 1, 2007.
34. N. Yoshikawa, "Fundamentals and applications of microwave heating of metals," *Journal of Microwave Power and Electromagnetic Energy*, 44 (1), 2010, pp. 4-13.
35. http://home.clara.net/rod.beavon/err_comb.htm
36. Li-Yang Shao, Y. Shevchenko and J. Albert, "Intrinsic temperature sensitivity of tilted fiber Bragg grating based surface plasmon resonance Sensors," *Optics Express*, vol. 18, no. 11, 24 May 2010.

37. M. Iga, A. Sekib, K. Watanabe, "Gold thickness dependence of SPR-based hetero-core structured optical fiber sensor," *Sensors and Actuators*, B 106 (2005) 363–368.
38. E. Maxwell, "Conductivity of metallic surfaces at microwave frequencies," *Journal of Applied Physics*, vol. 18, no. 7, July, 1947.
39. H. Suzuki, M. Sugimoto, Y. Matsui, J. Kondoh, "Effects of gold film thickness on spectrum profile and sensitivity of a multimode-optical-fiber SPR sensor," *Sensors and Actuators*, B 132 (2008) 26–33.
40. M. Iga, A. Sekib, K. Watanabe, "Gold thickness dependence of SPR-based hetero-core structured optical fiber sensor," *Sensors and Actuators*, B 106 (2005) 363–368.
41. E. Maxwell, "Conductivity of metallic surfaces at microwave frequencies," *Journal of Applied Physics*, Vol. 18, No. 7, July, 1947.
42. Anuj K Sharma and B D Gupta, "Fibre-optic sensor based on surface plasmon resonance with Ag–Au alloy nanoparticle films," *Nanotechnology* 17 (2006) 124–131.
43. I. Del Villar, C. R. Zamarreño, M. Hernaez, F.J. Arregui, and Ignacio R. Matias, , "Lossy Mode Resonance Generation With Indium-Tin-Oxide-Coated Optical Fibers for Sensing Applications," *Journal of Lightwave Technology*, Vol. 28, No. 1, January 1, 2010.
44. Raman Kashyap, *Fiber Bragg Gratings*, Academic Press.
45. Barbora Spacková, Marek Piliarik, Pavel Kvasnicka, Christos Themistos, Muttukrishnan Rajarajan, J. Homola, "Novel concept of multi-channel fiber optic surface plasmon resonance sensor", *Sensors and Actuators B* , 139 (2009) pp.199–203.
46. B.E.A. Saleh, M.C.Teich, *Fundamentals of Photonics*, Second Edition, Wiley & Sons, Canada, 2007. Ch.2.
47. H.K.Raut, V.A. Ganesh, A.S. Nair and S. Ramakrishna, "Anti-reflective coatings: A critical, in-depth review", *Energy Environ. Sci.*, 2011, 4, 3779. www.rsc.org/ees.
48. I. Hodgkinson, Q.H. Wu, "Anisotropic antireflection coatings: design and fabrication", *Optics Letters*, Vol. 23, No. 19, October 1998, pp. 1553-1555.
49. L. Atternas, L. Thylen, "Single-Layer Antireflection Coating of Semiconductor Lasers: Polarization Properties and the Influence of the Laser Structure", *Journal of Lightwave Tech.*, Vol.7, No.2, February 1989, pp.426-430.
50. R.E.Smith, M.E.Warren, J.R. Wendt and G.A. Vawter, "Polarization-sensitive subwavelength antireflection surfaces on a semiconductor for 975 nm", *Optics Letters*, Vol.21, No.15, August 1996, pp. 1201-1203.
51. R.R.Willey, "Non-Polarizing Beamsplitter and AR Coating Design", *Proceedings of the Society of Vacuum Coaters on 48th Annual Technical Conference*, 2005, ISSN-0737-5921, pp.391-395.
52. I. Yamada, K.Kintaka, J.Nishii, S.Akioka, Y. Yamagishi and M. Saito, "Transmittance enhancement of a wire-grid polarizer by antireflection coating", *Applied Optics*, Vol.48, No.2, January 2009, pp. 316-320.
53. J.A.Dobrowolski, J.E.Ford, B.T.Sullivan, L.Lu and N.R. Osborne, "Conducting antireflection coatings with low polarization dependent loss for telecommunication applications", *Optics Express*, Vol. 12 Issue.25, 2004, pp. 6258-6269.
54. P. Yeh, *Optical Waves in Layered Media*, John Wiley and Sons, 1988.
55. R. Baets, *Photonics Syllabus*, Universiteit Gent, 2006.
56. B.E.A. Saleh, M.C.Teich, *Fundamentals of Photonics*, Second Edition, Wiley & Sons, Canada, 2007. Ch.2.
57. I. Hodgkinson, Q.H. Wu, "Anisotropic antireflection coatings: design and fabrication", *Optics Letters*, Vol. 23, No. 19, October 1998, pp. 1553-1555.
58. I.G.Kavakli, K.Kantarli, "Single and Double Layer Antireflection Coatings on Silicon", *Turk J Phys*, 26 (2002), pp. 349-354.

59. I. Khan, "Polarization Effect of Antireflection Coating for SOI Material System", *International Journal of Science and Research*, Vol.1, Issue 3, pp. 59-63.
60. L. Atternas, L. Thylen, "Single-Layer Antireflection Coating of Semiconductor Lasers: Polarization Properties and the Influence of the Laser Structure", *Journal of Lightwave Tech.*, Vol.7, No.2, February 1989, pp.426-430.
61. R.R.Willey, "Non-Polarizing Beamsplitter and AR Coating Design", *In Proceedings of the Society of Vacuum Coaters on 48th Annual Technical Conference*, 2005, ISSN-0737-5921, pp.391-395.
62. I.Yamada, K.Kintaka, J.Nishii, S.Akioka, Y. Yamagishi and M. Saito, "Transmittance enhancement of a wire-grid polarizer by antireflection coating", *Applied Optics*, Vol.48, No.2, January 2009, pp. 316-320.
63. J.A.Dobrowolski, J.E.Ford, B.T.Sullivan, L.Lu and N.R. Osborne, "Conducting antireflection coatings with low polarization dependent loss for telecommunication applications", *Optics Express*, Vol. 12 Issue.25, 2004, pp. 6258-6269.
64. H. A. Macleod, *Thin-film Optical Filters*, 2nd edn, McGraw-Hill, 1989.
65. www.mellesgriot.com-Technical Information.
66. Tuan Guo, Hwa-Yaw Tam, Jacques Albert, "Linearly chirped and weakly tilted fiber Bragg grating edge filters for in-fiber sensor interrogation" *Proc. of SPIE*, Vol. 7753, 77537V-1, 2011.
67. Hidekazu Sueyoshi and Shigeki Kakiuchi, "Microwave Heating of Thin Au Film", *Materials Transactions*, Vol. 48, No. 3, 2007, pp. 531-537.
68. M.Navarrete, N. Diaz-Herrera, A. Gonzalez-Cano and O. Esteban, "A polarization-independent SPR fiber sensor", *Plasmonics* (2010) 5, Springer, pp. 7-12.
69. Weigang Ma, Xing Zhang and Koji Takahashi, "Electrical properties and reduced Debye temperature of polycrystalline thin gold films", *J. Phys. D: Appl. Phys.* 43 (2010) 465301 (8pp), doi:10.1088/0022-3727/43/46/465301
70. K.L. Chopra, L.C. Bobb, and M.H. Francombe, "Electrical Resistivity of Thin Single-Crystal Gold Films", *Journal of Applied Physics*, Vol. 34, No. 6, June 1963, pp. 1699-1702.